

# Petrology and *in situ* U–Th–Pb Monazite Geochronology of Ultrahigh-Temperature Metamorphism from the Andriamena Mafic Unit, North–Central Madagascar. Significance of a Petrographical $P$ – $T$ Path in a Polymetamorphic Context

PHILIPPE GONCALVES<sup>1\*</sup>, CHRISTIAN NICOLLET<sup>1</sup> AND JEAN-MARC MONTEL<sup>2</sup>

<sup>1</sup>LABORATOIRE MAGMAS ET VOLCANS, UNIVERSITÉ BLAISE PASCAL–CNRS, 5, RUE KESSLER, 63038 CLERMONT-FERRAND CEDEX, FRANCE

<sup>2</sup>LMTG, UNIVERSITÉ PAUL SABATIER–CNRS, 14, AVENUE EDOUARD BELIN, 31400

RECEIVED FEBRUARY 4, 2003; ACCEPTED APRIL 14, 2004

*Petrological studies and electron microprobe dating of monazite from the mafic Andriamena unit, north–central Madagascar, indicate that an apparently continuous P–T path inferred for Mg–granulites is actually discontinuous, resulting from the superposition of two distinct metamorphic events at 2.5 Ga and ~750 Ma. The late Archaean event corresponds to an ultrahigh-temperature metamorphism (1000°C, 10.5 kbar) characterized by a sapphirine–garnet–orthopyroxene–quartz assemblage. Neoproterozoic ages are associated with the development of a sapphirine–cordierite-bearing assemblage, symplectites of orthopyroxene–sillimanite and partial melting at ~850°C and 7 kbar. This sequence of reactions and mineral assemblages could be interpreted as the result of near-isothermal decompression to about 4 kbar followed by isobaric cooling to 650°C. However, geodynamic constraints suggest that the granulites underwent a phase of cooling to the stable geotherm following the ultrahigh-temperature metamorphism at 2.5 Ga. Consequently, we suggest that the ‘petrographical path’ inferred from the Mg–granulites is not representative of the actual P–T–t path. The decompression, in particular, is an artefact of the P–T path with no geological meaning; it results from the equilibration of the refractory late Archaean ultrahigh-temperature assemblages at a lower pressure during the middle Neoproterozoic event.*

KEY WORDS: *Andriamena unit; Madagascar, ultrahigh-temperature metamorphism; electron microprobe dating of monazite; polymetamorphism; P–T–t path*

## INTRODUCTION

Determining accurate  $P$ – $T$ – $t$  paths is fundamental to discussing and understanding the nature and timing of orogenic processes. The combination of petrological and geochronological studies of rocks that have recorded the metamorphic evolution of a high-grade gneiss terrain is essential to unravel its evolution. In recent years, ultrahigh-temperature (UHT) granulites have been discovered in numerous gneiss terrains [see review by Harley (1998a)]. Such rocks have attracted petrologists’ attention because they preserve assemblages, such as sapphirine–quartz, that reflect extreme  $P$ – $T$  conditions (>1050°C, 8–13 kbar). Furthermore, owing to their refractory nature, these rocks commonly preserve a complex history in their numerous and spectacular coronitic and symplectitic textures, which can be described in a simple (K)FMASH chemical system (McDade & Harley, 2001). Combining interpretations of reaction textures with

\*Corresponding author. Present address: Department of Geosciences, University of Massachusetts, 611 North Pleasant Street, Amherst, MA 01003-9297, USA. Telephone: 413-545-0745. Fax: 413-545-1200. E-mail: philippe@geo.umass.edu

appropriate experimentally calibrated petrogenetic grids (Hensen, 1986; Hensen & Harley, 1990; Bertrand *et al.*, 1991; Audibert *et al.*, 1995; Carrington & Harley, 1995) provides powerful information with which to reconstruct qualitative or semi-quantitative parts of the  $P$ – $T$  path close to the peak metamorphic temperature (Droop, 1989; Harley, 1998*b*; Kriegsman & Schumacher, 1999; McDade & Harley, 2001).

Complex  $P$ – $T$  paths have been inferred, with a very high degree of confidence, from numerous UHT granulite localities. However, in areas that have a polymetamorphic history [e.g. Napier complex and Rauer group in Antarctica (Harley *et al.*, 1990; Harley, 1998*b*); Okiep copper district in South Africa (Raith & Harley, 1998); Eastern Ghats in India (Bose *et al.*, 2000; Rickers *et al.*, 2001)], some uncertainties remain with respect to the timing of the different parts of these  $P$ – $T$  paths. Without geochronological constraints on the absolute timing of the different periods of mineral assemblage growth, reaction textures formed during different thermal events can be erroneously ascribed to a single event (Hand *et al.*, 1992; Vernon, 1996). The superposition of at least two separate thermal events could lead to either a discontinuous or an apparent  $P$ – $T$  path with no real geological significance, and thus to misinterpretation.

This study focuses on the petrology and textural evolution of a suite of UHT Mg-rich granulites from north-central Madagascar and associated migmatites, allowing construction of petrography-based  $P$ – $T$  paths. The absolute age for the  $P$ – $T$ – $t$  path was obtained by U–Th–Pb electron microprobe (EMP) dating of monazite. Because of its *in situ* nature and high spatial resolution, this technique allows dating of grains in their petrographical context and consequently the linking of ages with metamorphic mineral assemblages (Montel *et al.*, 1996; Williams *et al.*, 1999). Particular attention has been given to the relationships between the age and chemical composition of the monazite [U, Th, Pb and rare earth elements (REE)–P–Ca–Si–Y] to reveal distinct episodes of monazite crystallization.

## GEOLOGICAL SETTING

North-central Madagascar records a long and complex late Archaean to late Neoproterozoic magmatic and metamorphic history (Caen-Vachette, 1979; Guérrot *et al.*, 1993; Nicollet *et al.*, 1997; Paquette & Nédélec, 1998; Tucker *et al.*, 1999; Kröner *et al.*, 2000; Goncalves *et al.*, 2003). Its basement consists of two main lithotectonic units: a gneissic–granitic domain and an overlying mafic sequence corresponding to the ‘Beforona group’ of Bésairie (1963) or the ‘Tsaratana thrust sheet’ of Collins *et al.* (2000).

The gneissic–granitic domain consists of late Archaean granites and gneisses (2550–2500 Ma) that were

deformed and metamorphosed at 820–720 Ma, 630 Ma and 550–500 Ma; periods that correspond to widespread granitic plutonism. The ‘Beforona group’ consists of three north–south-trending elongate mafic units (Maevatanana unit, Andriamena unit and Aloatra–Beforona unit from west to east), which lie structurally above the gneissic–granitic domain (Fig. 1a). The Andriamena unit, the focus of this study, forms a large synform separated from the underlying basement by a major mylonitic zone (Goncalves *et al.*, 2003). It includes reworked late Archaean mafic and biotite-bearing gneisses and metapelitic migmatites (garnet–sillimanite-bearing rocks) intruded by voluminous mafic to ultramafic rocks at *c.* 790 Ma (Guérrot *et al.*, 1993) (Fig. 1b). This mafic magmatism has been correlated with widespread magmatic activity at ~820–720 Ma reported within the gneissic–granitic domain, which is interpreted as the result of a phase of continental arc magmatism related to the closure of the Mozambique Ocean (Handke *et al.*, 1999; Tucker *et al.*, 1999; Kröner *et al.*, 2000). Finally, the Andriamena unit, as all Madagascar, experienced multiple deformation events during the late Neoproterozoic to Cambrian (550–500 Ma) under amphibolite- to granulite-facies conditions (Martelat *et al.*, 2000; Goncalves *et al.*, 2003). At that time the Andriamena unit was emplaced onto the gneissic–granitic domain as the result of east–west horizontal shortening during the final amalgamation of Gondwana (Goncalves *et al.*, 2003).

## OUTCROP DESCRIPTION

Mg-granulites, including sapphirine-bearing gneiss, orthopyroxene–sillimanite–quartz gneisses and orthoamphibole–cordierite-bearing gneiss, account for a very small volume in the Andriamena unit. They have been reported in the central part near the villages of Andriamena and Brieville (Nicollet, 1990) and at the western margin of the unit north of the village of Andranomiely Sud (M. Ohnenstetter, personal communication, 2001) (Fig. 1b). Because of very poor exposure, detailed structural relationships between the Mg-granulites and gneissic basement are scarce. However, locally the Mg-granulites occur as lenses within a composite gneissic foliation composed of tonalitic and granodioritic gneisses with pelitic migmatites and mafic gneisses (Fig. 2a).

Mg-granulites (sapphirine-bearing samples: A4-5, A4-11, A4-26, C21, C43, C38; orthopyroxene–sillimanite–quartz-bearing samples: A4-31, C17) were collected 4 km east of the village of Andriamena [location (i) in Fig. 1b]. The outcrop is composed of interlayered amphibolitic gneiss, biotite gneiss, meta-Banded Iron Formation and migmatite that define a north–south-striking foliation. The metapelitic migmatites studied are well exposed just south of the Mg-granulite outcrop [see location (ii) in

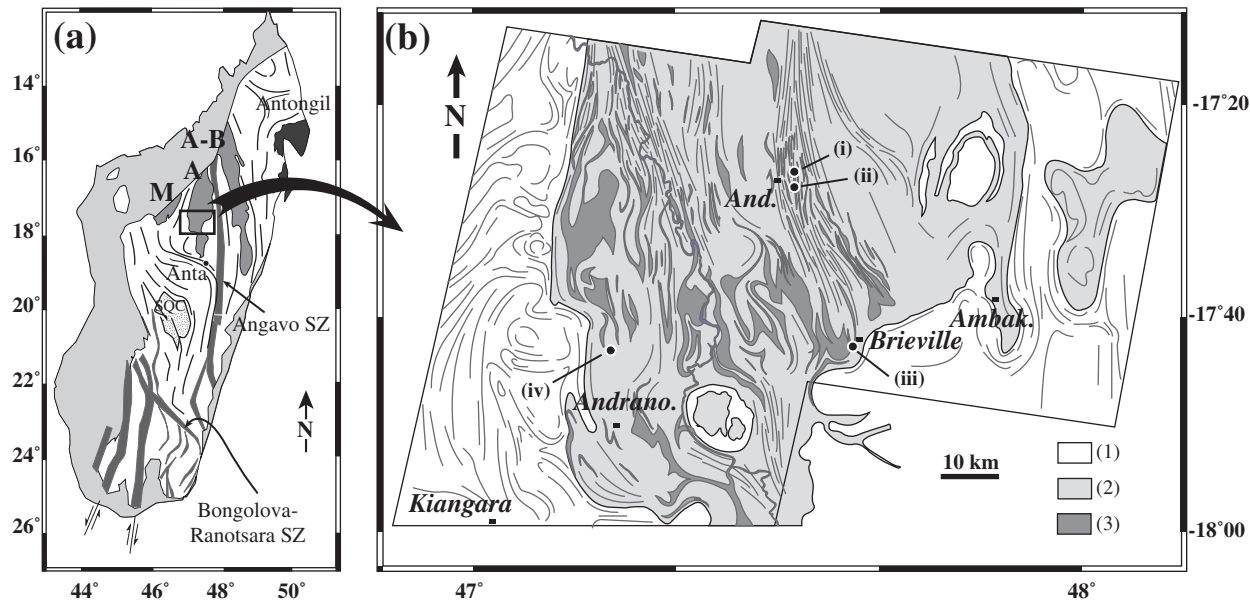


**Fig. 1.** (a) Simplified geological map of Madagascar illustrating the main structural and lithological features [modified after Martelat (1998)] and showing the location of the study area. The Maevatanana unit (M), Andriamena unit (A) and Aloatra-Beforona unit (A-B) form part of the ‘Beforona group’ of Bésairie (1963) or the ‘Tsaratanana thrust sheet’ of Collins *et al.* (2000). (b) Simplified geological map of a part of the Andriamena unit and surrounding basement, showing the main structural orientations (Goncalves *et al.*, 2003) and the sample locations. (1) Late Archaean to late Neoproterozoic gneissic-granitic reworked basement; (2) late Archaean Andriamena unit (mafic gneisses, biotite gneisses, migmatites); (3) middle Neoproterozoic mafic-ultramafic intrusions. Sample locations: (i) samples A4-5, A4-11, A4-26, A4-31, C17, C21, C38 and C43; (ii) C61; (iii) An4c and A6-3; (iv) opx-sil-qtz-bearing rocks location (M. Ohnenstetter, personal communication, 2001). And., Andriamena; Ambak., Ambakireny; Andrano., Andranomiely sud; SZ, shear zone.

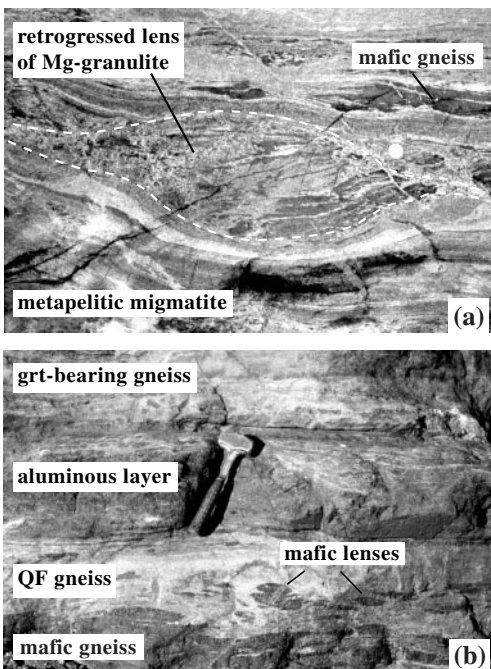


**Fig. 2.** Outcrop photographs of the Mg-granulites and migmatites. (a) Detail of a lens of strongly retrogressed Mg-granulite-bearing gneiss hosted within migmatitic metasediments. (b) Pelitic migmatite composed of an alternation of quartzofeldspathic leucosomes (QF) containing mafic lenses (lower half of photograph) with an aluminous quartz-absent layer and garnet-bearing gneiss layer.

Fig. 1b], where they display a well-developed layering consisting of quartzofeldspathic leucosomes, boudined mafic gneiss, garnet-bearing gneiss and aluminous quartz-absent layers (Fig. 2b). Samples from the Brieville locality are dominated by orthoamphibole-cordierite-bearing granulites (An4c, A6-3), which have been collected close to the quarry of Ankazotaolana, 2 km west of the village of Brieville [see location (iii) in Fig. 1b]. The outcrop that contains the lens of orthoamphibole-bearing gneiss consists predominantly of orthopyroxene-bearing leucogneiss with quartzite and numerous lenses of metabasic rocks (amphibole + plagioclase and relict orthopyroxene).

## PETROGRAPHY AND MINERAL CHEMISTRY

### Mg-granulites (sapphirine-bearing and orthopyroxene-sillimanite-bearing gneisses)

Mg-granulites from the Andriamena locality are coarse grained. The mineral associations are complex, including four generations of orthopyroxene and two generations of garnet, sapphirine and sillimanite. Quartz, spinel, plagioclase and biotite are also present. Porphyroblasts of garnet commonly exceeding 2 cm in diameter, occur in

Table 1: Summary of the mineral assemblages and textural features in the Mg-granulites from Andriamena

	Mineral associations					Reaction textures												
	Grt	Opx	Spr	Sil	Crd	Stage 1 (UHT)			Stage 2 (ITD)				Stage 3 (IBC)					
						1	2	3	4	5	7	8	9	10	11	12	4a	5a
<i>Qtz- and spr-bearing assemblages</i>																		
A4-11	1	1–2–3	1	0–1–3	2	X		X	X			X						X
A4-26	1	1–2–3	1	1–3	2	X	X	X	X			X						X
C21	1	1–2–3	1	1–3	2	X	X	X	X			X						X
<i>Qtz-free, spr-bearing assemblages</i>																		
C43	1	1–2–3	1–2	1–3	2			X		X			X		X	X		X
C38	1–2	1–2–3	1–2	1–3	2			X		X	X		X		X			
<i>Qtz-bearing, spr-free assemblages</i>																		
A4-5	1–2	1–2–3	(1)–2	1–3	2	(X)		X	X	X	X			X	X		X	X
C17	1	1–3	—	1–3	2				X					X				X
A4-31	1	2–3	—	1–3	2				X			X		X				X

In the following list, subscripts 1–2–3 correspond to the mineral generation. Reaction label same as in text: (1)  $\text{spr}_{1a} + \text{qtz} = \text{opx}_{1b} + \text{sil}_{1b}$ ; (2)  $\text{grt}_{1a} + \text{qtz} = \text{opx}_{1b} + \text{sil}_{1b}$ ; (3) Al-rich opx = opx + grt (exsolution); (4)  $\text{opx}_1 + \text{sil}_1 + \text{qtz} = \text{crd}_2$ ; (5)  $\text{opx}_1 + \text{sil}_1 = \text{spr}_2 + \text{crd}_2$ ; (6)  $\text{opx}_1 + \text{sil}_1 + \text{qtz} = \text{crd}_2$ ; (7)  $\text{opx}_1 + \text{sil}_1 = \text{spr}_2 + \text{crd}_2 + \text{grt}_2$ ; (8)  $\text{grt}_1 + \text{qtz} = \text{opx}_2 + \text{crd}_2$ ; (9)  $\text{grt}_1 + \text{sil}_1 + \text{qtz} = \text{crd}_2$ ; (10)  $\text{grt}_1 + \text{sil}_1 = \text{spr}_2 + \text{crd}_2$ ; (11)  $\text{grt}_1 = \text{opx}_2 + \text{spr}_2 + \text{crd}_2$ ; (12)  $\text{grt}_1 = \text{opx}_2 + \text{spl}_2 + \text{crd}_2$ ; (4a)  $\text{crd}_2 = \text{opx}_3 + \text{sil}_3 + \text{qtz}$ ; (5a)  $\text{spr}_2 + \text{crd}_2 = \text{opx}_3 + \text{sil}_3$ .

a groundmass of fine-grained prismatic orthopyroxene, sillimanite and locally quartz. Sapphirine occurs as prismatic crystals up to 5 mm in length (C43, C38, A4-26 A4-11), and as fine-grained intergrowths formed at the expense of the porphyroblast minerals (C38, A4-26, A4-5).

The eight samples described in this study (A4-5, A4-11, A4-26, A4-31, C17, C21, C43 and C38) have been subdivided into three types based on the occurrence of quartz and/or sapphirine as a primary high-grade metamorphic phase (Table 1). In the following discussion the numbers 1a, 1b, 2 and 3 associated with minerals refer to different generations of phases, which will be subsequently used to describe three specific stages (1, 2 and 3) of the  $P$ – $T$  evolution.

#### Preserved peak metamorphic assemblages

*Quartz- and sapphirine-bearing assemblages: garnet–orthopyroxene–sapphirine–sillimanite–quartz (A4-11, A4-26 and C21).* In these rocks, peak metamorphic minerals are never in mutual contact. Garnet ( $\text{grt}_{1a}$ ) is mainly pyrope–almandine, with  $X_{\text{Mg}} [\text{Mg}/(\text{Mg} + \text{Fe}^{2+})] = 0.57–0.51$  (Table 2), that forms medium to large corroded porphyroblasts up to 2 cm in diameter containing inclusions of sillimanite, quartz, rutile and sapphirine. Adjacent to quartz, they are surrounded by late-formed composite coronas. Primary

orthopyroxene ( $\text{opx}_{1a}$ ) forms large porphyroblasts up to 1 cm in diameter, which contain exsolution lamellae of garnet ( $X_{\text{Mg}} = 0.53–0.47$ , Table 3) (Fig. 3c) and inclusions of rutile. The orthopyroxene ( $\text{opx}_{1a}$ ) has a high alumina content (7.1–9.7 wt %) and  $X_{\text{Mg}}$  ranging from 0.73 to 0.81 (Table 3). The initial alumina content of  $\text{opx}_{1a}$  before extraction of alumina through garnet exsolution has been estimated to have been  $\sim 13$  wt % (Nicollet, 1990). Sapphirine ( $\text{spr}_{1a}$ ) ( $X_{\text{Mg}} = 0.76–0.84$ , Al 4.2–4.4 p.f.u.,  $\text{Cr}_2\text{O}_3 < 2.4$  wt %, Table 4) occurs as residual grains, containing inclusions of spinel ( $X_{\text{Mg}} < 0.50$ ,  $\text{Cr}_2\text{O}_3 \sim 2.3$  wt %, Table 5), separated from matrix quartz by a coronitic texture composed of sillimanite ( $\text{sil}_{1b}$ ) and orthopyroxene ( $\text{opx}_{1b}$ ) (Fig. 3a). Primary sapphirine is also characterized by  $\text{Cr}_2\text{O}_3$  contents up to 2.4 wt % (Table 4). Primary sillimanite ( $\text{sil}_{1a}$ ) occurs as large prismatic grains.

*Quartz-free assemblages: garnet–orthopyroxene–sapphirine ( $\pm$  sillimanite) (C43, C38).* Garnet ( $\text{grt}_{1b}$ ) ( $X_{\text{Mg}} = 0.60–0.56$ , Table 2) occurs as lobate porphyroblasts up to 2 cm in diameter, or granular areas, and locally contains inclusion trails of sillimanite, biotite and quartz, typically located in the central part of the crystal. Orthopyroxene ( $\text{opx}_{1b}$ ) ( $X_{\text{Mg}} = 0.75–0.80$ ,  $\text{Al}_2\text{O}_3$  7.5–9.2 wt %, Table 3) occurs as coarse porphyroblasts up to 20 mm in diameter or as recrystallized polygonal medium-sized grains in

Table 2: Representative electron microprobe analyses of garnet from Mg-granulites and the pelitic migmatite

Sample:	Mg-granulites										Metapelitic migmatite (C61)		
	C43 core	A4-11 core	A4-5 core	A4-31 core	C43 rim	A4-11 rim	A4-5 rim	A4-31 rim	C43 exsol.	A4-5 neo grt <sub>2</sub>	Layer A porph core	Layer B porph rim	neo grt
Analysis:	37	42	27	60	19	41	52	52	31	23	38	37	4
SiO <sub>2</sub>	40.43	39.32	39.67	39.33	39.95	38.61	40.42	39.53	39.79	39.23	39.17	38.96	38.60
TiO <sub>2</sub>	0.00	0.00	0.02	0.00	0.02	0.01	0.00	0.03	0.00	0.00	0.04	0.02	0.05
Al <sub>2</sub> O <sub>3</sub>	22.65	22.47	22.64	22.68	22.81	22.39	22.88	22.63	22.42	22.65	21.88	22.19	22.27
Cr <sub>2</sub> O <sub>3</sub>	0.00	0.09	n.d.	n.d.	0.02	0.14	n.d.	n.d.	0.02	0.00	0.27	0.17	0.00
Fe <sub>2</sub> O <sub>3</sub>	1.77	2.88	2.41	2.00	1.96	3.29	1.05	1.62	1.52	1.27	0.66	0.07	1.00
FeO	18.94	21.38	21.07	23.63	19.17	22.14	22.66	25.26	21.09	23.19	26.70	28.21	27.35
MnO	0.44	0.43	0.82	0.26	0.39	0.40	0.74	0.31	0.50	0.63	0.42	0.42	0.35
MgO	15.13	13.40	13.65	12.59	14.89	12.22	13.27	11.89	13.17	12.30	9.19	8.89	8.98
CaO	1.47	0.97	0.95	0.51	1.29	1.26	0.87	0.39	1.91	0.79	2.64	1.56	1.86
Na <sub>2</sub> O	0.01	0.00	0.00	0.01	0.01	0.05	0.02	0.00	0.01	0.02	0.00	0.02	0.02
K <sub>2</sub> O	0.03	0.02	0.00	0.00	0.00	0.00	0.02	0.00	0.00	0.01	0.00	0.01	0.00
Total	100.86	100.97	101.25	101.02	100.49	100.50	101.94	101.67	100.45	100.11	100.97	100.53	100.49
Si	2.97	2.93	2.94	2.94	2.95	2.91	2.98	2.96	2.97	2.96	2.99	2.99	2.96
Ti	0.00	0.00	0.00	0.00	0.00	0.00	0.00	0.00	0.00	0.00	0.00	0.00	0.00
Al	1.96	1.97	1.98	2.00	1.99	1.99	1.99	1.99	1.97	2.01	1.97	2.01	2.01
Cr	0.00	0.01	n.d.	n.d.	0.00	0.01	n.d.	n.d.	0.00	0.00	0.02	0.01	0.00
Fe <sup>3+</sup>	0.10	0.16	0.13	0.11	0.11	0.19	0.06	0.09	0.09	0.07	0.04	0.00	0.06
Fe <sup>2+</sup>	1.16	1.33	1.31	1.48	1.18	1.40	1.40	1.58	1.32	1.46	1.70	1.81	1.76
Mn	0.03	0.03	0.05	0.02	0.02	0.03	0.05	0.02	0.03	0.04	0.03	0.03	0.02
Mg	1.66	1.49	1.51	1.40	1.64	1.37	1.46	1.33	1.47	1.38	1.04	1.02	1.03
Ca	0.12	0.08	0.08	0.04	0.10	0.10	0.07	0.03	0.15	0.06	0.22	0.13	0.15
Na	0.00	0.00	0.00	0.00	0.00	0.01	0.00	0.00	0.00	0.00	0.00	0.00	0.00
K	0.00	0.00	0.00	0.00	0.00	0.00	0.00	0.00	0.00	0.00	0.00	0.00	0.00
Grossular	0.04	0.03	0.03	0.01	0.04	0.04	0.02	0.01	0.05	0.02	0.05	0.05	0.05
Almandine	0.39	0.46	0.44	0.50	0.40	0.48	0.47	0.53	0.44	0.50	0.57	0.61	0.59
Pyrope	0.56	0.51	0.51	0.48	0.56	0.47	0.49	0.45	0.49	0.47	0.35	0.34	0.35
Spessartine	0.01	0.01	0.02	0.01	0.01	0.01	0.02	0.01	0.01	0.01	0.01	0.01	0.01
X <sub>Mg</sub> (Fe <sup>2+</sup> )	0.59	0.53	0.54	0.49	0.58	0.50	0.51	0.46	0.53	0.49	0.37	0.38	0.36

n.d., not determined.

textural equilibrium with sapphirine. Orthopyroxene in the quartz-free assemblage also has garnet exsolution lamellae. Large prismatic crystals of sapphirine (spr<sub>1b</sub>), up to 10 mm in diameter, contain inclusions of garnet, cordierite, biotite and orthopyroxene. Garnet (grt<sub>1b</sub>) and sapphirine (spr<sub>1b</sub>) porphyroblasts are never in mutual contact. Prismatic sillimanite (sil<sub>1b</sub>) is less abundant and is separated from garnet (grt<sub>1b</sub>) and orthopyroxene (opx<sub>1b</sub>) by secondary corona textures.

*Sapphirine-free and quartz-bearing assemblages: garnet-orthopyroxene-sillimanite-quartz (C17, A4-5 and A4-31).* Sample C17 is composed mainly of coarse (up to 1 cm) sub- to

euhedral orthopyroxene (opx<sub>1b</sub>), prismatic sillimanite (sil<sub>1b</sub>) that occurs both in the matrix and as inclusions in orthopyroxene (opx<sub>1b</sub>), and quartz. The peak metamorphic assemblage (opx<sub>1b</sub>-sil<sub>1b</sub>-qtz) is well preserved; reaction textures are uncommon, except for a narrow corona of cordierite (crd<sub>2</sub>) between peak metamorphic phases. Garnet (grt<sub>1b</sub>) is present as a minor phase. Sample A4-5 shows the same peak metamorphic assemblage (opx<sub>1b</sub>-sil<sub>1b</sub>-qtz) in addition to local grt<sub>1b</sub>-opx<sub>1b</sub>-sil<sub>1b</sub>. Garnet (X<sub>Mg</sub> = 0.51-0.54, Table 2) occurs as widely corroded medium-grained porphyroblasts or as a residual phase located in retrograded symplectites.

Table 3: Representative electron microprobe analyses of orthopyroxene from Mg-granulites

Sample:	C43	C43	C21	A4-5	C38	C43	A4-11	A4-5
	opx <sub>1</sub>	opx <sub>1</sub>	opx <sub>1</sub> -sil	opx <sub>1</sub>	opx <sub>2</sub> -spr <sub>2</sub> -crd <sub>2</sub>	opx <sub>2</sub> -spl <sub>2</sub> -crd <sub>2</sub>	opx <sub>2</sub> -crd <sub>2</sub>	opx <sub>3</sub> -sil <sub>3</sub> (-qtz)
	porph core	grt contact	reaction (1)	porph rim	reaction (11)	reaction (12)	reaction (8)	reaction (4a)
Analysis:	63	24	101	2	94	46	51	7
SiO <sub>2</sub>	49.58	49.71	49.78	49.72	51.65	50.82	49.67	52.41
TiO <sub>2</sub>	0.07	0.18	0.10	0.17	0.06	0.18	0.11	0.04
Al <sub>2</sub> O <sub>3</sub>	8.77	9.17	7.77	8.91	7.69	7.75	7.15	4.40
Cr <sub>2</sub> O <sub>3</sub>	0.11	0.08	0.27	n.d.	0.02	0.00	0.30	0.00
Fe <sub>2</sub> O <sub>3</sub>	2.03	1.18	1.60	1.61	0.00	1.56	2.74	0.32
FeO	13.99	13.48	16.90	15.60	15.54	11.72	13.57	16.12
MnO	0.13	0.15	0.08	0.25	0.11	0.06	0.07	0.23
MgO	25.19	25.74	23.85	24.48	25.46	27.49	25.68	25.92
CaO	0.14	0.08	0.06	0.08	0.02	0.03	0.05	0.06
Na <sub>2</sub> O	0.03	0.00	0.01	0.01	0.00	0.02	0.01	0.01
K <sub>2</sub> O	0.01	0.00	0.01	0.00	0.04	0.00	0.00	0.00
Total	100.06	99.78	100.42	100.82	100.59	99.63	99.35	99.52
Si	1.78	1.78	1.81	1.79	1.85	1.81	1.80	1.90
Ti	0.00	0.00	0.00	0.00	0.00	0.00	0.00	0.00
Al	0.37	0.39	0.33	0.38	0.32	0.33	0.31	0.19
Cr	0.00	0.00	0.01	n.d.	0.00	0.00	0.01	0.00
Fe <sup>3+</sup>	0.05	0.03	0.04	0.04	0.00	0.04	0.07	0.01
Fe <sup>2+</sup>	0.42	0.40	0.51	0.47	0.46	0.35	0.41	0.49
Mn	0.00	0.00	0.00	0.01	0.00	0.00	0.00	0.01
Mg	1.35	1.38	1.29	1.31	1.36	1.46	1.39	1.40
Ca	0.01	0.00	0.00	0.00	0.00	0.00	0.00	0.00
Na	0.00	0.00	0.00	0.00	0.00	0.00	0.00	0.00
K	0.00	0.00	0.00	0.00	0.00	0.00	0.00	0.00
X <sub>Mg</sub> (Fe <sup>2+</sup> )	0.76	0.77	0.72	0.74	0.75	0.81	0.77	0.74

Garnet contains scarce spinel inclusions surrounded by sapphirine. Large polygonal orthopyroxene (opx<sub>1b</sub>) ( $X_{Mg} = 0.73-0.77$ , Al<sub>2</sub>O<sub>3</sub> 6.7–8.9 wt %, Table 3) contains inclusions of quartz and garnet exsolution. Orthopyroxene is always separated from sillimanite (sil<sub>1b</sub>) by late reaction textures. Sample A4-31 is characterized by a minor amount of orthopyroxene and by substantial retrogression. The peak metamorphic assemblage is grt<sub>1b</sub>-sil<sub>1b</sub>-qtz ± opx<sub>1b</sub>. Garnet (grt<sub>1b</sub>) ( $X_{Mg} = 0.49-0.46$ ) occurs as corroded porphyroblasts, which are not in contact with sillimanite (sil<sub>1b</sub>) and quartz.

#### Coronitic and symplectitic textures

The Al–Mg granulites preserve numerous coronitic and symplectitic structures involving cordierite (crd<sub>2</sub>), sapphirine (spr<sub>2</sub>) and orthopyroxene (opx<sub>1b</sub> and opx<sub>2</sub>). These minerals have a constant composition. Cordierite

(crd<sub>2</sub>) is the most magnesian mineral ( $X_{Mg} = 0.89-0.92$ , Table 6) and may contain minor amounts of H<sub>2</sub>O or CO<sub>2</sub> because its analytical total is about 98.5%. Coronitic sapphirine (spr<sub>2</sub>) is relatively more magnesian ( $X_{Mg} = 0.81-0.88$ , Table 4) and aluminous (Al ~4.4 p.f.u.) compared with early sapphirine (spr<sub>1a</sub> and spr<sub>1b</sub>). Secondary orthopyroxene (opx<sub>2</sub>) has a slightly lower alumina content of ~7–8 wt % and similar  $X_{Mg}$  values to early orthopyroxene (opx<sub>1a</sub> and opx<sub>1b</sub>, Table 3).

*Sapphirine–quartz destabilization.* In samples A4-11, A4-26 and C21, early sapphirine (spr<sub>1a</sub>) forms the core of the corona texture and is separated from matrix quartz by an orthopyroxene corona (opx<sub>1b</sub>) ( $X_{Mg} = 0.74-0.76$ , Al<sub>2</sub>O<sub>3</sub> 6.2–7.5 wt %) with a constant thickness adjacent to quartz and prismatic sillimanite (sil<sub>1b</sub>) next to sapphirine (Fig. 3a). In sample A4-5, sapphirine is not present, but is interpreted to have been completely consumed by a similar reaction (Fig. 3d). In the three samples, orthopyroxene

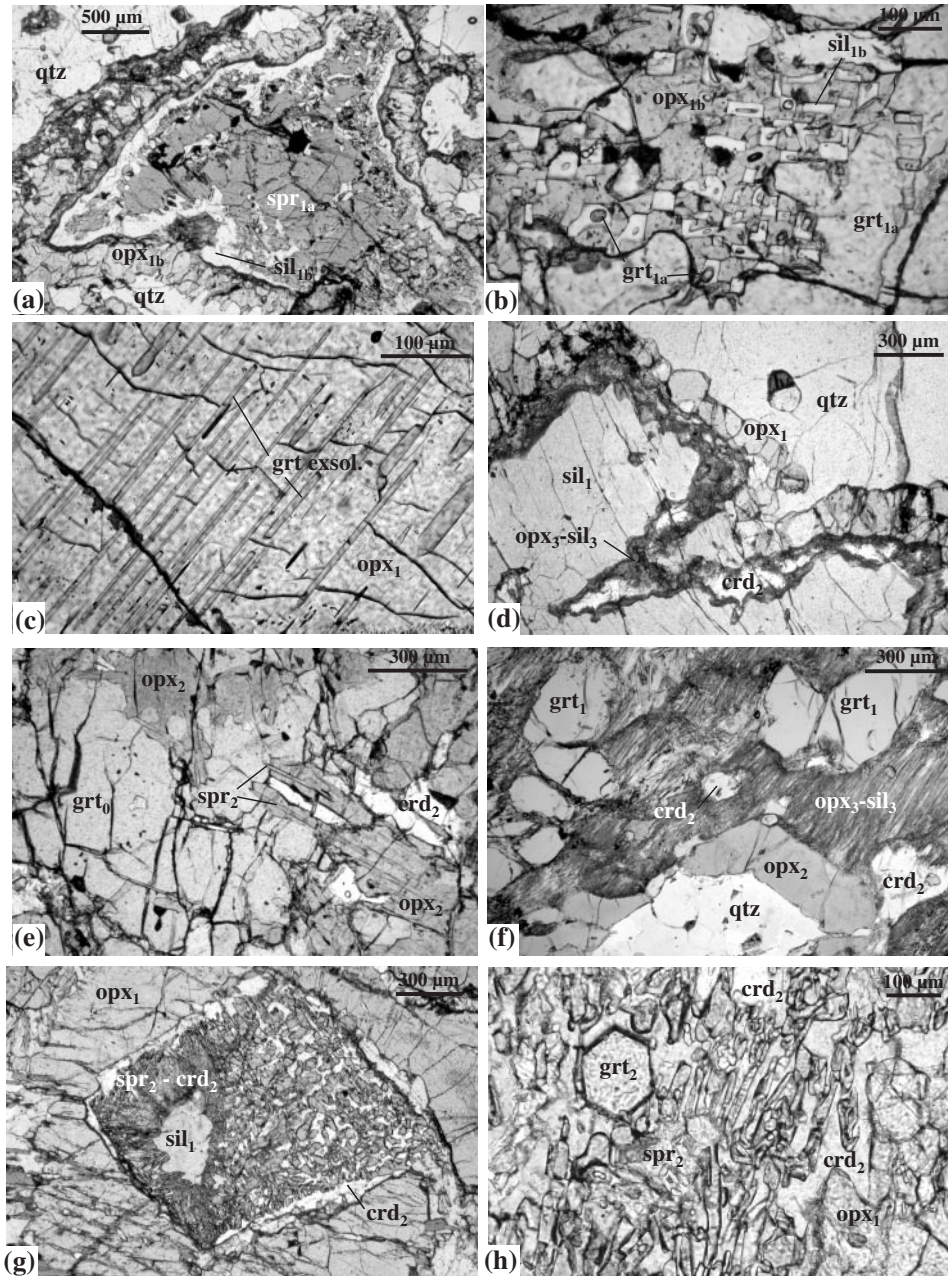


**Fig. 3.** Selected photomicrographs illustrating the retrograde reactions observed in the Mg-granulites from Andriamena. (a) Sample A4-26. Evidence of a primary sapphirine ( $\text{spr}_{1a}$ )–quartz assemblage. Such phases are no longer in mutual contact, but they are separated by a corona of  $\text{opx}_{1b}$  adjacent to quartz and prismatic  $\text{sil}_{1b}$  next to  $\text{spr}_{1a}$  suggesting the reaction (1)  $\text{spr}_{1a} + \text{qtz} = \text{opx}_{1b} + \text{sil}_{1b}$ . It should be noted that  $\text{opx}_{1b}$  and  $\text{sil}_{1b}$  are also separated by a very fine crystallized assemblage as in (d). (b) Sample A4-26. Garnet ( $\text{grt}_{1a}$ ) crack filled by an  $\text{opx}_{1b}$ – $\text{sil}_{1b}$  symplectite. Sillimanite occurs as small euhedral prismatic crystals, which can contain relics of  $\text{grt}_{1a}$ . This symplectite is consistent with the reaction  $\text{grt}_{1a} + \text{qtz} = \text{opx}_{1b} + \text{sil}_{1b}$ . (c) Sample A4-26. Orthopyroxene porphyroblast ( $\text{opx}_1$ ) containing exsolution lamellae of garnet. (d) Sample A4-5. Prismatic  $\text{sil}_1$  surrounded by coronitic  $\text{opx}_1$  at the contact of quartz. This texture suggests that the peak metamorphic assemblage was sapphirine–quartz but all the sapphirine has been completely consumed by the reaction (1).  $\text{Opx}_1$  is separated from  $\text{sil}_1$  by a narrow corona of  $\text{crd}_2$  produced by the reaction (4)  $\text{opx}_1 + \text{sil}_1 + \text{qtz} = \text{crd}_2$ . It should be noted that the  $\text{crd}_2$  is also partly retrogressed into a very fine symplectite developed along the grain boundaries. Such symplectite is composed of  $\text{opx}_3$ – $\text{sil}_3 \pm \text{qtz}$  suggesting the reverse reaction (4a)  $\text{crd}_2 = \text{opx}_3 + \text{sil}_3 + \text{qtz}$ . (e) Sample A4-5. Lamellar intergrowth of  $\text{spr}_2$  and  $\text{opx}_2$  associated with minor  $\text{crd}_2$  produced at the expense of  $\text{grt}_1$  via the reaction (11)  $\text{grt}_1 = \text{opx}_2 + \text{spr}_2 + \text{crd}_2$ . (f) Sample A4-31. Relics of an early  $\text{grt}_1$  separated from quartz by a composite corona of  $\text{opx}_2$  and  $\text{crd}_2$  presumably formed through the reaction (8)  $\text{grt}_1 + \text{qtz} = \text{opx}_2 + \text{sil}_1 + \text{qtz} = \text{crd}_2$ . The cordierite ( $\text{crd}_2$ ) is subsequently widely replaced by needles of  $\text{sil}_3$  and  $\text{opx}_3$  as in (a) and (d) through the reaction (4a)  $\text{crd}_2 = \text{opx}_3 + \text{sil}_3 \pm \text{qtz}$ . (g) Sample C43. Large porphyroblast of  $\text{opx}_1$  with a former prismatic inclusion of  $\text{sil}_1$  almost replaced by a sapphirine–cordierite symplectite. It indicates the decompression reaction (5)  $\text{opx}_1 + \text{sil}_1 = \text{spr}_2 + \text{crd}_2$ . (h) Sample C38.  $\text{Spr}_2$ – $\text{crd}_2$  symplectite associated with euhedral garnet ( $\text{grt}_2$ ) produced at the expense of  $\text{opx}_1$  and  $\text{sil}_1$  (not visible in this photograph) via the invariant reaction (spl–qtz) (7)  $\text{opx}_1 + \text{sil}_1 = \text{grt}_2 + \text{spr}_2 + \text{crd}_2$ .

Table 4: Representative electron microprobe analyses of sapphirine from Mg-granulites

Sample:	C43	A4-11	C43	C38	A4-5
	spr <sub>1</sub>	spr <sub>0</sub>	opx <sub>2</sub> –spr <sub>2</sub> –crd <sub>2</sub>	spr <sub>2</sub> –crd <sub>2</sub>	spr <sub>2</sub> –crd <sub>2</sub>
	porph	porph	reaction (11)	reaction (10)	reaction (5)
Analysis:	26	1	45	73	17
SiO <sub>2</sub>	13.76	13.14	12.79	13.16	12.77
TiO <sub>2</sub>	0.09	0.04	0.02	0.10	0.00
Al <sub>2</sub> O <sub>3</sub>	61.53	60.31	63.14	62.93	62.91
Cr <sub>2</sub> O <sub>3</sub>	0.12	2.42	0.10	0.11	0.11
Fe <sub>2</sub> O <sub>3</sub>	1.15	1.44	1.39	0.30	1.72
FeO	6.19	6.67	4.29	6.86	6.13
MnO	0.02	0.02	0.02	0.00	0.03
MgO	17.04	16.30	17.44	16.17	16.39
CaO	0.01	0.00	0.01	0.06	0.00
Na <sub>2</sub> O	0.02	0.00	0.00	0.03	0.01
K <sub>2</sub> O	0.00	0.01	0.02	0.01	0.00
Total	99.94	100.35	99.22	99.73	100.09
Si	0.82	0.79	0.76	0.78	0.76
Ti	0.00	0.00	0.00	0.00	0.00
Al	4.30	4.25	4.42	4.41	4.40
Cr	0.01	0.11	0.00	0.01	0.01
Fe <sup>3+</sup>	0.05	0.06	0.06	0.01	0.08
Fe <sup>2+</sup>	0.31	0.33	0.21	0.34	0.30
Mn	0.00	0.00	0.00	0.00	0.00
Mg	1.51	1.45	1.54	1.43	1.45
Ca	0.00	0.00	0.00	0.00	0.00
Na	0.00	0.00	0.00	0.00	0.00
K	0.00	0.00	0.00	0.00	0.00
X <sub>Mg</sub> (Fe <sup>2+</sup> )	0.83	0.81	0.88	0.81	0.83

(opx<sub>1b</sub>) and sillimanite (sil<sub>1b</sub>) are no longer in mutual contact (Fig. 3a and d).

*Garnet breakdown.* In the quartz-bearing samples (A4-26 and C21), fractures in large garnet porphyroblasts are filled with a very fine symplectite composed of orthopyroxene (opx<sub>1b</sub>) and sillimanite (sil<sub>1b</sub>) (Fig. 3b). Garnet is surrounded by an almost continuous corona of orthopyroxene (opx<sub>2</sub>) and cordierite (crd<sub>2</sub>) and/or plagioclase (An50, Table 7) that separates garnet from matrix quartz. Sillimanite (sil<sub>1b</sub>) occurs as euhedral prisms, which contain inclusions of garnet (grt<sub>1a</sub>) (Fig. 3b). Cordierite (crd<sub>2</sub>) typically occurs between garnet (grt<sub>1a</sub>) and orthopyroxene (opx<sub>2</sub>) (Fig. 3f). In most quartz-bearing samples, garnet and sillimanite are separated by cordierite (crd<sub>2</sub>). In quartz-free samples, garnet (grt<sub>1b</sub>) is separated from sillimanite (sil<sub>1b</sub>) by a sapphirine–cordierite or –plagioclase (An85–90, Table 7) symplectite. Sapphirine (spr<sub>2</sub>) occurs as 300 μm long vermicular grains intergrown with cordierite (crd<sub>2</sub>). Locally a fine lamellar intergrowth of

orthopyroxene (opx<sub>2</sub>) and sapphirine (spr<sub>2</sub>) with minor cordierite (crd<sub>2</sub>) composes the rims of corroded garnet (Fig. 3e). This symplectite also fills garnet fractures, and in one sample (C43) sapphirine is replaced by vermicular spinel (spl<sub>2</sub>) ( $X_{Mg} > 0.53$  and  $Cr_2O_3 < 0.5$  wt %, Table 5) forming an opx<sub>2</sub>–spl<sub>2</sub>–crd<sub>2</sub> symplectite.

*Orthopyroxene–sillimanite breakdown.* In the quartz-bearing assemblages (A4-11, C21, C17, A4-5, A4-26 and A4-31), orthopyroxene (opx<sub>1a</sub> and opx<sub>1b</sub>) is separated from sillimanite by a narrow monomineralic corona of cordierite (crd<sub>2</sub>) (Fig. 3d). In samples or layers lacking quartz (C43, C38 and A4-5), they are separated by a sapphirine–cordierite symplectite (spr<sub>2</sub>–crd<sub>2</sub>). Locally, the sapphirine–cordierite symplectite may mimic the former prismatic sillimanite (Fig. 3g). In these textures, sapphirine is separated from orthopyroxene by cordierite. Plagioclase (An85–90, Table 7) may occur in the spr<sub>2</sub>–crd<sub>2</sub> symplectites (C43). Rarely, the breakdown of the assemblage orthopyroxene (opx<sub>1a</sub> and opx<sub>1b</sub>)–sillimanite produces

Table 5: Representative electron microprobe analyses of spinel from Mg-granulites and the pelitic migmatite

Sample:	Mg-granulites			Migmatite	
	C21 relics in spr <sub>0</sub>	C43 spl <sub>2</sub> -crd <sub>2</sub> reaction (5)	C43 opx <sub>2</sub> -spl <sub>2</sub> -crd <sub>2</sub> reaction (12)	Al-rich layer B matrix	matrix
Analysis:	99	57	43	1	25
SiO <sub>2</sub>	0.08	0.01	0.04	0.00	0.00
TiO <sub>2</sub>	0.00	0.00	0.03	0.00	0.02
Al <sub>2</sub> O <sub>3</sub>	61.18	62.67	63.56	59.90	58.85
Cr <sub>2</sub> O <sub>3</sub>	2.28	0.43	0.17	0.81	1.18
Fe <sub>2</sub> O <sub>3</sub>	0.00	0.00	0.00	2.44	2.99
FeO	22.67	20.08	15.14	24.69	26.70
MnO	0.05	0.02	0.03	0.00	0.00
ZnO	n.d.	n.d.	n.d.	1.33	1.13
MgO	11.82	12.49	16.07	9.76	8.77
CaO	0.00	0.05	0.00	0.04	0.03
Na <sub>2</sub> O	0.00	0.00	0.02	0.06	0.00
K <sub>2</sub> O	0.01	0.00	0.02	0.01	0.01
Total	98.08	95.76	95.07	99.04	99.69
Si	0.00	0.00	0.00	0.00	0.00
Ti	0.00	0.00	0.00	0.00	0.00
Al	1.96	2.02	2.01	1.94	1.91
Cr	0.05	0.01	0.00	0.02	0.03
Fe <sup>3+</sup>	0.00	0.00	0.00	0.05	0.06
Fe <sup>2+</sup>	0.51	0.46	0.34	0.57	0.62
Mn	0.00	0.00	0.00	0.00	0.00
Zn	n.d.	n.d.	n.d.	0.03	0.02
Mg	0.48	0.51	0.64	0.40	0.36
Ca	0.00	0.00	0.00	0.00	0.00
Na	0.00	0.00	0.00	0.00	0.00
K	0.00	0.00	0.00	0.00	0.00
X <sub>Mg</sub> (Fe <sup>2+</sup> )	0.48	0.53	0.65	0.41	0.37

spr<sub>2</sub>-crd<sub>2</sub> symplectites with minor crystallization of euhedral garnet (A4-5, C38) (Fig. 3f).

*Late cordierite breakdown.* Cordierite (crd<sub>2</sub>) displays late partial to complete replacement by a very fine-grained symplectite (Fig. 3d). The nature of the symplectite varies with respect to its position. Near porphyroblasts of garnet (grt<sub>1a</sub> and grt<sub>1b</sub>) or orthopyroxene (opx<sub>1a</sub>, opx<sub>1b</sub> or opx<sub>2</sub>), it consists of an intergrowth of randomly oriented needles of sillimanite (sil<sub>3</sub>) and orthopyroxene (opx<sub>3</sub>) (Fig. 4a). Close to the porphyroblasts of sillimanite (sil<sub>1</sub>), the symplectite is composed of vermicular quartz and euhedral prismatic sillimanite (sil<sub>3</sub>) included in orthopyroxene (opx<sub>3</sub>) and forming a graphic texture (Fig. 4b). Quartz is always located close to the earlier sillimanite. Another characteristic is the conspicuous Al-poor composition of

the orthopyroxene (~4 wt %), and low X<sub>Mg</sub> (0.71–0.76) compared with earlier generations (Table 3).

### Mg-granulites (orthoamphibole-bearing gneisses)

The petrography of the orthoamphibole-bearing granulites (An4c and A6-3) from the Brieville locality was described in detail by Nicollet (1988) and is briefly summarized here. These rocks consist mainly of garnet, orthopyroxene, cordierite, orthoamphibole, biotite, ilmenite, sillimanite and quartz.

The peak metamorphic assemblage in sample An4c is partly retrogressed and consists of relict garnet, orthopyroxene, rare sillimanite and abundant quartz,

Table 6: Representative electron microprobe analyses of cordierite from Mg-granulites

Sample:	C38	A4-5	C38	C21	A4-5
	spr <sub>2</sub> —crd <sub>2</sub>	spr <sub>2</sub> —crd <sub>2</sub>	opx <sub>2</sub> —spr <sub>2</sub> —crd <sub>2</sub>	opx <sub>2</sub> —crd <sub>2</sub>	crd <sub>2</sub>
	reaction (10)	reaction (5)	reaction (11)	reaction (8)	reaction (4)
Analysis:	72	15	86	116	66
SiO <sub>2</sub>	49.89	50.41	50.04	48.87	50.19
TiO <sub>2</sub>	0.01	0.00	0.05	0.00	0.00
Al <sub>2</sub> O <sub>3</sub>	33.81	33.85	33.74	33.58	33.94
Cr <sub>2</sub> O <sub>3</sub>	0.01	0.00	0.02	0.00	0.00
FeO	2.46	2.02	2.15	2.33	2.61
MnO	0.03	0.00	0.05	0.01	0.04
MgO	12.16	12.61	12.38	12.30	12.42
CaO	0.00	0.00	0.04	0.00	0.02
Na <sub>2</sub> O	0.03	0.06	0.05	0.02	0.07
K <sub>2</sub> O	0.02	0.00	0.00	0.00	0.00
Total	98.42	98.96	98.52	97.11	99.29
Si	4.99	5.01	4.99	4.94	4.99
Ti	0.00	0.00	0.00	0.00	0.00
Al	3.98	3.96	3.97	4.00	3.97
Cr	0.00	0.00	0.00	0.00	0.00
Fe <sup>2+</sup>	0.21	0.17	0.18	0.20	0.22
Mn	0.00	0.00	0.00	0.00	0.00
Mg	1.81	1.87	1.84	1.85	1.84
Ca	0.00	0.00	0.00	0.00	0.00
Na	0.01	0.01	0.01	0.00	0.01
K	0.00	0.00	0.00	0.00	0.00
X <sub>Mg</sub> (Fe <sup>2+</sup> )	0.90	0.92	0.91	0.90	0.89

forming a recrystallized polygonal granoblastic mosaic. Porphyroblasts of orthopyroxene are partially or completely replaced by orthoamphibole. Orthopyroxene contains garnet exsolution lamellae, like the primary orthopyroxene (opx<sub>1a</sub> and opx<sub>1b</sub>) observed in the Mg-granulites from the Andriamena locality (Fig. 5a). Peak metamorphic garnet occurs as partially resorbed porphyroblasts located in aggregates of orthoamphibole–cordierite ± biotite (Fig. 5b). Sillimanite occurs as inclusions in garnet porphyroblasts or small needles in quartz grain boundaries.

Sample A6-3 is strongly retrogressed and displays heterogeneous deformation. In the less deformed areas, orthopyroxene occurs as megacrysts containing inclusions of euhedral orthoamphibole, quartz and ilmenite. Garnet is significantly less abundant than orthopyroxene and occurs as porphyroblasts with numerous inclusions of quartz. A foliation, which warps the porphyroblasts of orthopyroxene and garnet, is defined by the preferential orientation of orthoamphibole, elongate cordierite and monocrystalline quartz ribbons. An important feature of

sample A6-3 is that cordierite contains orthoamphibole and sillimanite, which are never in mutual contact and display evidence of resorption. Late staurolite has been observed locally in association with cordierite.

### Pelitic migmatite

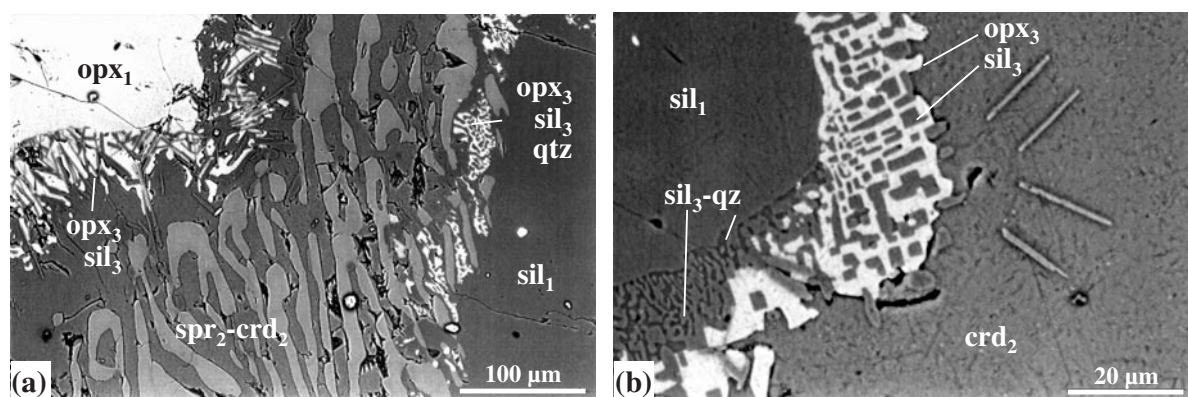
Sample C61 is a pelitic migmatite showing a layering, which consists of an alternation of restite (mesosome) and quartzofeldspathic layers (segregated leucosome) at a centimetre to millimetre scale (Fig. 6). Four different layers (assemblages A–D) have been distinguished at the sample scale (Fig. 6).

#### Silica-saturated layer (assemblage A)

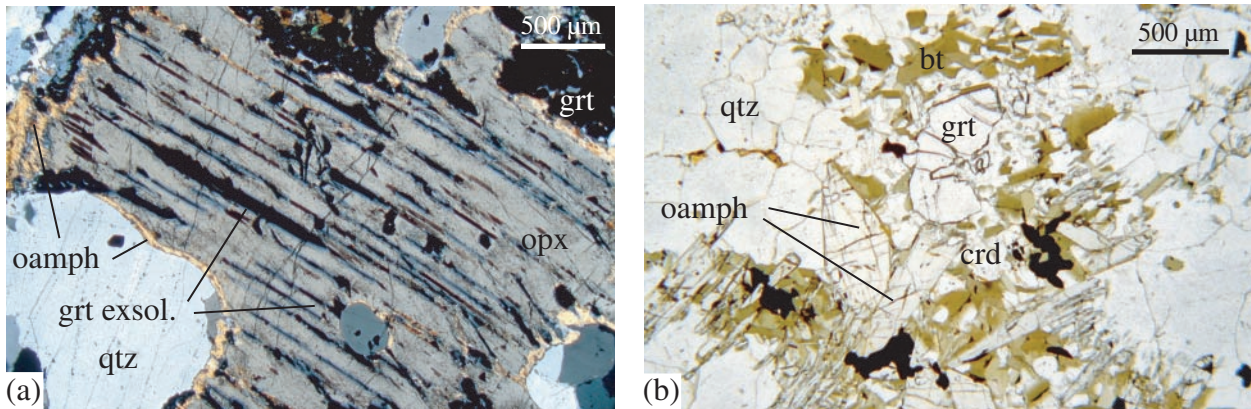
The silica-saturated layer in the mesosome contains abundant garnet, biotite, plagioclase and quartz with accessory monazite and zircon. Garnet forms subhedral to euhedral porphyroblasts (up to 50 µm) with numerous fine-grained inclusions of biotite ( $X_{Mg} = 0.84–0.85$ ),

Table 7: Representative electron microprobe analyses of plagioclase from Mg-granulites and the pelitic migmatite

Sample:	Mg-granulites		Metapelitic migmatite (C61)					
	C43	C43	Silica sat. layer (A)		Al-rich layer (A)			
Analysis:	opx <sub>2</sub> -pl <sub>2</sub>	spr <sub>2</sub> -crd <sub>2</sub> /pl <sub>2</sub>	matrix	i. grt	matrix	matrix	i. grt	i. spl
	5	50	41	40	21	22	30	27
SiO <sub>2</sub>	56.34	43.66	57.68	55.93	55.37	47.94	53.79	55.51
TiO <sub>2</sub>	0.00	0.00	0.00	0.00	0.00	0.02	0.04	0.04
Al <sub>2</sub> O <sub>3</sub>	27.49	35.28	26.85	27.19	28.05	32.01	27.37	27.57
Cr <sub>2</sub> O <sub>3</sub>	0.01	0.02	0.00	0.00	0.02	0.00	0.05	0.08
Fe <sub>2</sub> O <sub>3</sub>	0.06	0.45	0.02	0.04	0.09	0.15	0.62	0.43
MnO	0.00	0.01	0.00	0.01	0.00	0.01	0.00	0.00
MgO	0.00	0.40	0.00	0.01	0.00	0.00	0.09	0.02
CaO	9.79	18.70	9.11	9.75	10.67	16.04	10.28	9.93
Na <sub>2</sub> O	6.28	0.98	6.71	6.17	5.86	2.51	5.86	5.91
K <sub>2</sub> O	0.11	0.00	0.13	0.10	0.03	0.03	0.35	0.13
Total	100.08	99.52	100.53	99.20	100.12	98.70	98.45	99.66
Si	2.52	2.02	2.57	2.53	2.49	2.22	2.46	2.51
Ti	0.00	0.00	0.00	0.00	0.00	0.00	0.00	0.00
Al	1.45	1.92	1.41	1.45	1.48	1.75	1.47	1.47
Cr	0.00	0.00	0.00	0.00	0.00	0.00	0.00	0.00
Fe <sup>3+</sup>	0.00	0.02	0.00	0.00	0.00	0.01	0.02	0.01
Mn	0.00	0.00	0.00	0.00	0.00	0.00	0.00	0.00
Mg	0.00	0.03	0.00	0.00	0.00	0.00	0.01	0.00
Ca	0.47	0.93	0.43	0.47	0.51	0.80	0.50	0.48
Na	0.55	0.09	0.58	0.54	0.51	0.23	0.52	0.52
K	0.01	0.00	0.01	0.01	0.00	0.00	0.02	0.01
An	0.46	0.91	0.43	0.46	0.50	0.78	0.48	0.48
Ab	0.53	0.09	0.57	0.53	0.50	0.22	0.50	0.52
Or	0.01	0.00	0.01	0.01	0.00	0.00	0.02	0.01



**Fig. 4.** Backscattered electron images of the very fine symplectites  $\text{opx}_3\text{-sil}_3 \pm \text{qtz}$  produced at the expense of  $\text{crd}_2$  through the reverse reaction (4a)  $\text{crd}_2 = \text{opx}_3 + \text{sil}_3 \pm \text{qtz}$ . (a) Sample A4-5.  $\text{Spr}_2\text{-crd}_2$  developed at the expense of  $\text{opx}_1\text{-sil}_1$  through the reaction (5)  $\text{opx}_1 + \text{sil}_1 = \text{spr}_2 + \text{crd}_2$ . The  $\text{crd}_2$  is replaced at its grain boundaries by  $\text{opx}_3$  (white) and  $\text{sil}_3$  (black). It should be noted that next to the  $\text{opx}_1$  porphyroblast,  $\text{sil}_3$  occurs as randomly oriented needles intergrown with  $\text{opx}_3$ , whereas it forms small euhedral prisms next to the  $\text{sil}_1$  [see (b)]. (b) Sample A4-5. Detail of the  $\text{opx}_3\text{-sil}_3\text{-qtz}$  symplectite developed close to the  $\text{sil}_1$ .  $\text{Sil}_3$  included in the  $\text{opx}_3$  is characterized by its euhedral form and is also associated with vermicular quartz.



**Fig. 5.** Photographs showing textures of the orthoamphibole–cordierite-bearing gneisses from the Brieville locality. (a) Sample An4c. Exsolution of garnet in an orthopyroxene porphyroblast partly retrogressed into orthoamphibole. The occurrence of garnet exsolution suggests that orthoamphibole-bearing rocks had undergone UHT metamorphism. (b) Sample An6e. Relics of garnet in an aggregate composed of cordierite, orthoamphibole, and biotite at the contact of quartz. Such texture suggests the reaction  $\text{grt} + \text{qtz} = \text{oamph} + \text{crd}$ .

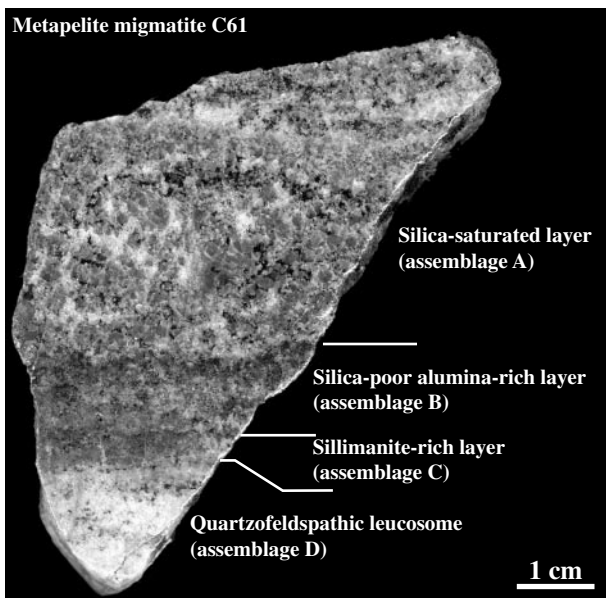


**Fig. 6.** Photograph of the pelitic migmatite C61 from the Andriamena locality showing the layered structure at a centimetre to millimetre scale, which consists of an alternation of restitic layers (assemblages A and B) with a leucosome (assemblage D). The sillimanite-rich layer (assemblage C) separates the quartzofeldspathic leucosome (assemblage D) from the silica-poor alumina-rich layer (assemblage B).

plagioclase (An40–47) and quartz. Biotite ( $X_{\text{Mg}} = 0.70\text{--}0.84$ ,  $\text{TiO}_2$  3.2–4.0 wt %, Table 8) in this quartz-bearing layer occurs mostly as aggregates of large laths in contact with garnet.

#### *Silica-poor alumina-rich layer (assemblage B)*

The transition between the silica-saturated layer and the silica-poor layer is sharp. The quartz-free layer is 1 cm wide and composed of garnet, spinel, ilmenite,

corundum, sillimanite, biotite and plagioclase. Garnet occurs as two habits: (1) euhedral to subhedral crystals of  $\sim 100\ \mu\text{m}$  in diameter ( $X_{\text{Mg}} = 0.36\text{--}0.38$  with a slight zoning, characterized by a decrease of  $X_{\text{Mg}}$  from core to rim) with rounded inclusions of biotite ( $X_{\text{Mg}} = 0.84\text{--}0.93$ ,  $\text{TiO}_2$  2.4–3.9 wt %, Table 8), plagioclase (An48–80, Table 7) and rare sillimanite (Fig. 7a); (2) small euhedral crystals ( $< 20\ \mu\text{m}$ ) ( $X_{\text{Mg}} = 0.36\text{--}0.38$ , Table 2) that are free of inclusions. Green spinel ( $X_{\text{Mg}} = 0.37\text{--}0.47$ ,  $\text{Cr}_2\text{O}_3$   $< 2.2$  wt % and  $\text{ZnO}$   $< 2.4$  wt %) is the conspicuous phase in assemblage B. It occurs as euhedral to subhedral grains ( $< 50\ \mu\text{m}$ ) intergrown with plagioclase, and contains the same rounded inclusions as those observed in the type-1 garnet (i.e. biotite, plagioclase and sillimanite) (Fig. 7a). Spinel rarely occurs as inclusions in garnet rims or it may be enclosed by garnet (Fig. 7b); it typically coexists with irregular grains of ilmenite and tabular corundum (Fig. 7c). These minerals are mostly surrounded by a narrow corona of sillimanite (Fig. 7b and c). With decreasing distance towards the leucosome (layer D), sillimanite increases in abundance at the expense of spinel. Near the sillimanite-rich layer (C), sillimanite occurs as prisms that may contain inclusions of spinel, and that are in textural equilibrium with biotite (Fig. 7d). Biotite ( $X_{\text{Mg}} = 0.77\text{--}0.85$ ,  $\text{TiO}_2$  3.2–4.0 wt %, Table 8) is less abundant than in the silica-saturated layer and occurs as small laths scattered in the layer and associated with sillimanite (Fig. 7d).

#### *Sillimanite-rich ( $\pm$ ilmenite, biotite) layer (assemblage C)*

This 5 mm wide layer separates the silica-undersaturated layer (B) from the quartzofeldspathic leucosome (D) (Fig. 6). It is essentially a sillimanite aggregate, with interstitial ilmenite and rarely biotite. The contact between

Table 8: Representative electron microprobe analyses of biotite from the pelitic migmatite

Metapelitic migmatite (C61)					
Sample:	Silica sat. layer A		Al-rich layer B		
	matrix	i. grt	matrix	i. grt	i. spl
Analysis:	41	39	27	16	39
SiO <sub>2</sub>	37.87	39.18	37.73	37.33	37.23
TiO <sub>2</sub>	3.98	2.42	3.55	3.93	1.43
Al <sub>2</sub> O <sub>3</sub>	16.28	16.43	16.51	17.15	18.19
Cr <sub>2</sub> O <sub>3</sub>	0.34	0.49	0.10	0.15	0.04
Fe <sub>2</sub> O <sub>3</sub>	3.00	1.40	3.70	5.10	2.98
FeO	7.76	6.54	7.35	3.81	6.39
MnO	0.00	0.00	0.00	0.02	0.00
ZnO	n.d.	0.00	n.d.	0.01	n.d.
MgO	16.37	19.29	16.93	18.37	19.57
CaO	0.02	0.03	0.00	0.02	0.00
Na <sub>2</sub> O	0.14	0.33	0.18	0.31	0.20
K <sub>2</sub> O	9.79	9.36	9.77	9.84	10.18
F	0.26	n.d.	0.33	n.d.	0.47
H <sub>2</sub> O	4.01	4.19	3.99	4.20	3.96
Total	99.81	99.65	100.14	100.24	100.65
Si	2.75	2.80	2.73	2.67	2.67
Ti	0.22	0.13	0.19	0.21	0.08
Al	1.39	1.39	1.41	1.44	1.54
Cr	0.02	0.03	0.01	0.01	0.00
Fe <sup>3+</sup>	0.16	0.08	0.20	0.27	0.16
Fe <sup>2+</sup>	0.47	0.39	0.44	0.23	0.38
Mn	0.00	0.00	0.00	0.00	0.00
Zn	n.d.	0.00	n.d.	0.00	n.d.
Mg	1.77	2.06	1.82	1.96	2.09
Ca	0.00	0.00	0.00	0.00	0.00
Na	0.02	0.05	0.03	0.04	0.03
K	0.91	0.85	0.90	0.90	0.93
F	0.06	n.d.	0.08	n.d.	0.11
H	1.94	2.00	1.92	2.00	1.89
X <sub>Mg</sub> (Fe <sup>2+</sup> )	0.79	0.84	0.80	0.90	0.85

the sillimanite layer and the quartzofeldspathic leucosome is sharp.

#### *Quartzofeldspathic leucosome (assemblage D)*

The leucosome consists of coarse-grained quartz, plagioclase, K-feldspar, garnet, ilmenite and minor biotite. Quartz displays undulatory extinction with prismatic sub-grain development. Plagioclase occurs as large polygonal crystals also with an undulatory extinction. Garnet is rare and occurs as small subhedral grains up to 100  $\mu\text{m}$

in diameter. It is nearly inclusion-free except for rare quartz and it is partially replaced by biotite.

## INTERPRETATION OF REACTION TEXTURES

### **Mg-granulites: FMAS(H) system**

A reaction texture sequence inferred from partial pseudomorphs and coronitic textures can be modelled in a

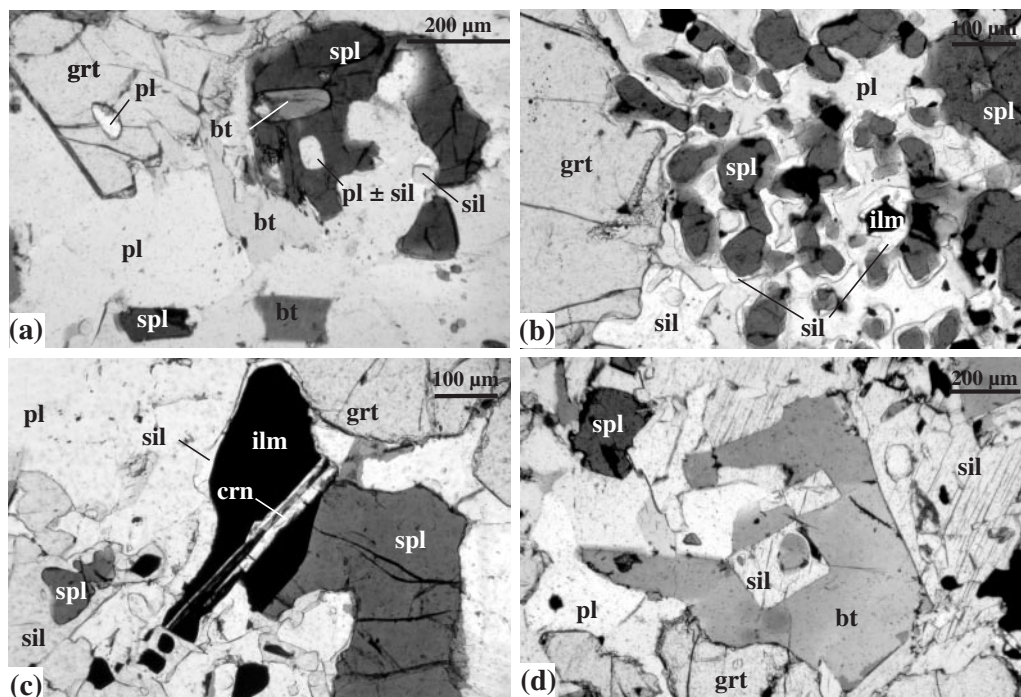
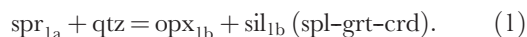


**Fig. 7.** Selected photomicrographs illustrating the petrographic features of the quartz-free, alumina-rich layer observed in the pelitic migmatite (C61). (a) Garnet and spinel containing relics of rounded inclusions of plagioclase, biotite and sillimanite, suggesting that such garnet and spinel correspond to incongruent phases produced during prograde biotite dehydration melting reactions. Biotite, sillimanite and plagioclase also occur in the matrix. (b) Aggregate of spinel surrounded by sillimanite. (c) Composite aggregate of spinel, ilmenite and lamellae corundum. Such phases are partly surrounded by a narrow corona of sillimanite at the contact of plagioclase. In the lower left part of the microphotograph, sillimanite is better developed and forms prisms with relic inclusions of spinel and ilmenite. Such late development of sillimanite at the expense of spinel and ilmenite is interpreted as a back melting reaction (see text for further explanation). (d) Late prismatic sillimanite in textural equilibrium with biotite. Such textures produced by back melting reactions are better developed close to the quartzofeldspathic leucosome.

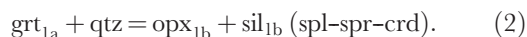
simple FMAS(H) system. Divariant reactions are illustrated using qualitative SFM projections from sillimanite and AFM projections from quartz (Fig. 8). Although all samples studied show evidence of distinct re-equilibration, textures in the rock suggest that the primary assemblages were  $\text{grt-spr-q-sil}$  or  $\text{grt-spr-opx-sil}$ .

#### *Destabilization of the initial peak metamorphic assemblage*

In the quartz-bearing samples, orthopyroxene ( $\text{opx}_{1b}$ ) and sillimanite ( $\text{sil}_{1b}$ ) coronas around sapphirine ( $\text{spr}_{1a}$ ) + quartz (Fig. 3a) suggest that the peak metamorphic assemblage is destabilized through the continuous reaction (Fig. 8b)

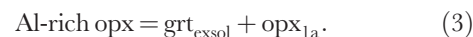


$\text{Opx}_{1b}$  and  $\text{sil}_{1b}$  also occur very locally in some garnet ( $\text{grt}_{1a}$ ) fractures in the presence of quartz (A4-26 and A4-11) (Fig. 3b), suggesting the continuous reaction



Reactions (1) and (2) can progress under the same  $P$ - $T$  conditions until the MAS reaction sapphirine + quartz = enstatite + sillimanite is crossed (Fig. 8b). When this

happened, the new stable assemblages would be  $\text{opx-sil-qtz-grt}$  and  $\text{opx-spr-grt-sil}$  (Fig. 8c). Formation of garnet exsolution lamellae in  $\text{opx}_{1a}$  (Fig. 3c) through reaction (3) (Nicollet, 1990) is also ascribed to this first stage following peak metamorphism:



#### *Secondary reaction textures: orthopyroxene ( $\text{opx}_{1a-1b}$ ) and garnet ( $\text{grt}_{1a-1b}$ ) breakdown*

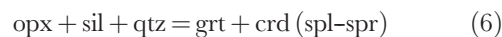
The early orthopyroxene ( $\text{opx}_{1a}$  and  $\text{opx}_{1b}$ ) is separated from sillimanite by cordierite in quartz-bearing and sapphirine-cordierite symplectites in quartz-free samples (Fig. 3d-g). This suggests the two continuous Fe-Mg reactions



and



These divariant reactions, like reaction (2), are co-stable until the univariant reaction



is crossed (Fig. 8d). In quartz-free domains, the sapphirine-cordierite symplectite may be associated with

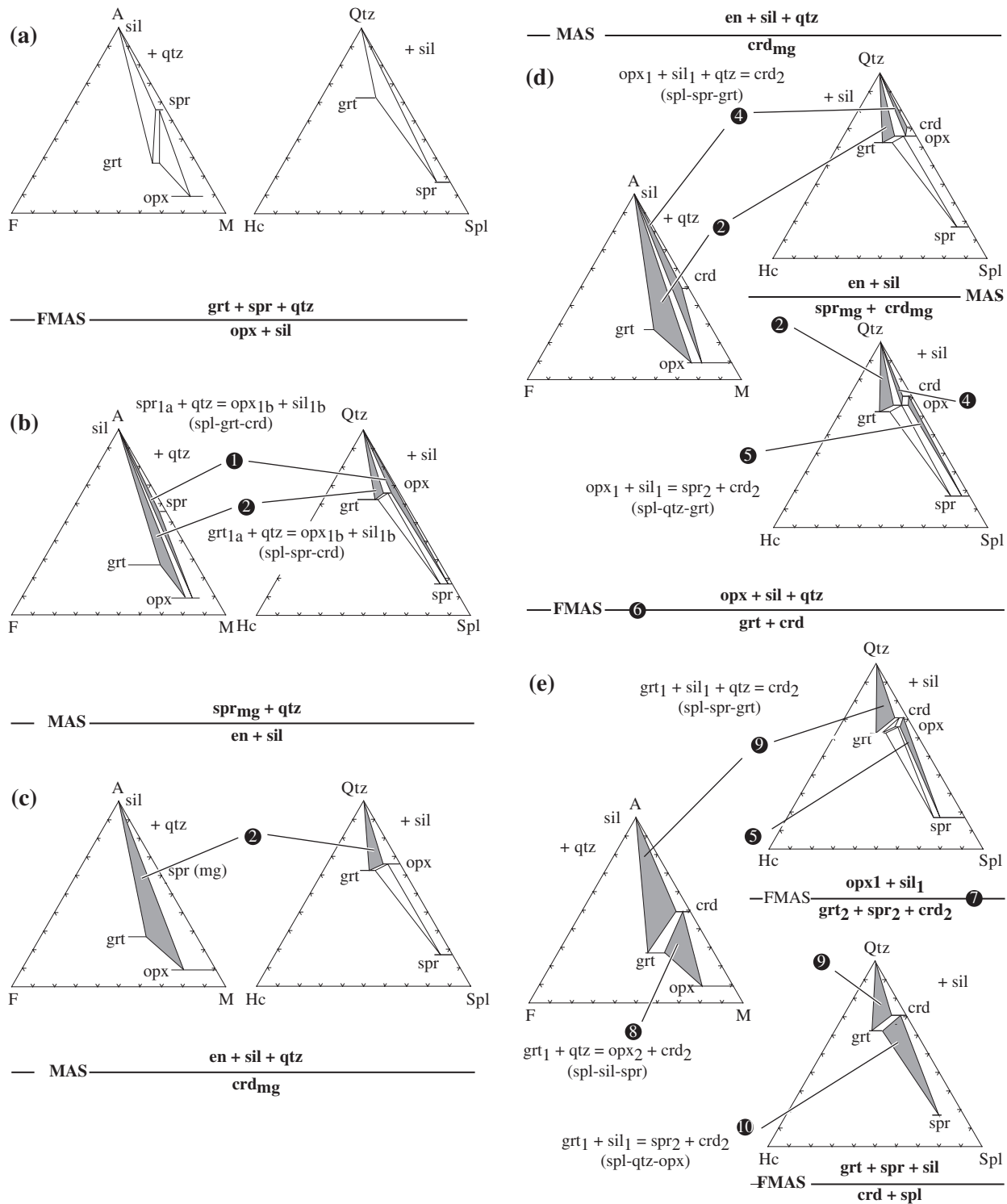
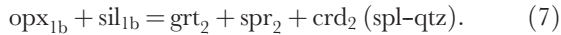


**Fig. 8.** Ideal series of AFM projections from quartz and Qtz–Hc–Spl projections from sillimanite, for the *P*–*T* path represented in the FMAS petrogenetic grid (Fig. 9), for stages 0, 1 and 2. The final stage (3) corresponding to the breakdown of cordierite into orthopyroxene–sillimanite symplectites is not represented. The projections show the sequence of continuous and discontinuous reactions deduced from the textural relationships observed in the Mg–granulites. Continuous and discontinuous reactions with quartz and sillimanite absent, such as reactions (11) and (12), cannot be represented in such a sequence as the diagrams are projected from quartz or sillimanite. Numbers in circles refer to reactions given in the text. Grey triangular areas correspond to continuous Fe–Mg reactions. For AFM projections: A = (Al + Cr + Fe<sup>3+</sup>)/2; F = Fe<sup>2+</sup>; M = Mg. For Qtz–Hc–Spl projections: Qtz = Si + Fe + Mg–Al/2; Hc = Fe<sup>2+</sup>; Spl = Mg.

small neoformed euhedral garnet (Fig. 3h). This texture is consistent with the discontinuous reaction

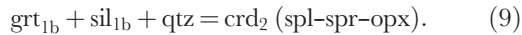


When this univariant reaction (7) is crossed, the continuous Fe–Mg reaction (5) is no longer stable.

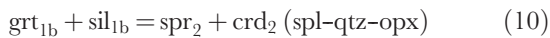
Garnet porphyroblasts display extensive resorption produced by various continuous reactions. As discussed in the above section, in quartz-bearing rocks garnet was destabilized into an orthopyroxene–sillimanite ( $\text{opx}_1\text{-sil}_1$ ) assemblage through reaction (2) until the univariant reaction (6) was crossed. Then, the newly stable continuous reaction involving the breakdown of the garnet–quartz assemblage was (Fig. 8e)



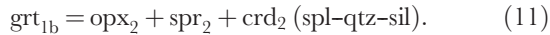
which produced the orthopyroxene–cordierite coronitic assemblage separating garnet from quartz (Fig. 3f). Such a reaction sequence [reaction (2) followed by (8)] is consistent with the observation of  $\text{opx}_1\text{-sil}_1$  symplectite in garnet fractures and  $\text{opx}_2\text{-crd}_2$  symplectite surrounding the same garnet and isolating  $\text{opx}_1\text{-sil}_1$  symplectite from the matrix. The occurrence of cordierite ( $\text{crd}_2$ ) between garnet and sillimanite in quartz-bearing rocks is consistent with the continuous reaction



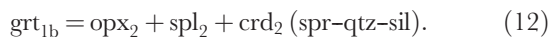
In quartz-free samples, a sapphirine–cordierite assemblage, similar to the one produced by reaction (5), separates garnet from sillimanite. This texture is consistent with the continuous reaction



which occurred after univariant reaction (7) was crossed. Fine lamellar intergrowth of orthopyroxene and sapphirine with minor cordierite developed at the expense of garnet porphyroblasts (Fig. 3e), suggesting the continuous reaction



Because neither quartz nor sillimanite is in excess in this reaction, it cannot be represented in Fig. 8. Locally, in sample C43, garnet fractures are filled by an orthopyroxene–spinel–cordierite symplectite, consistent with the continuous reaction

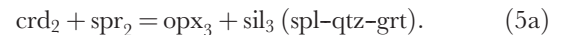
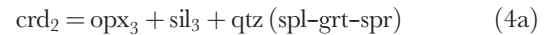


In all of these sites, orthopyroxene ( $\text{opx}_{1a-1b-2}$ ) has an alumina content  $>7$  wt %. This kind of secondary reaction sequence has been described in many other ultra-high-temperature terranes such as in Enderby Land and

the Rauer group, Antarctica (Harley *et al.*, 1990; Harley, 1998b), central Sri Lanka (Kriegsman & Schumacher, 1999), southern India (Raith *et al.*, 1997) and in the Limpopo belt, Zimbabwe (Hisada & Miyano, 1996).

#### *Textures post-dating the formation of cordierite ( $\text{crd}_2$ )*

Cordierite ( $\text{crd}_2$ ) produced by the breakdown of primary orthopyroxene and garnet was subsequently partially replaced by a very fine symplectite composed of an intergrowth of orthopyroxene–sillimanite  $\pm$  quartz (Figs 3d and f, and 4). Textural relationships suggest that this symplectite was produced by the reverse of reactions (4) and (5):



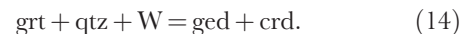
Orthopyroxene ( $\text{opx}_3$ ) thus produced is characterized by relatively low alumina content ( $\sim 4$  wt %). Such partial replacement of cordierite by an anhydrous symplectite composed of orthopyroxene and sillimanite has been described in aluminous granulites from Labwor Hills, Uganda (Sandiford *et al.*, 1987) and in the Arunta complex, central Australia (Goscombe, 1992). Typically, breakdown of cordierite involves hydration reactions leading to a gedrite + kyanite–sillimanite + quartz assemblage (Vernon, 1972; Van Reenen, 1986).

#### **Mg-granulites (orthoamphibole-bearing gneisses): FMASH system**

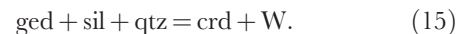
In the orthoamphibole-bearing gneisses, the partial replacement of peak metamorphic orthopyroxene by anthophyllite is consistent with the hydration reaction



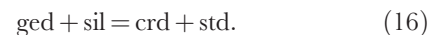
Strongly resorbed garnet porphyroblasts are separated from quartz by an assemblage of gedrite + cordierite (Fig. 5b), suggesting the reaction



In the quartz-bearing sample A6-3, the occurrence of cordierite containing relicts of gedrite and sillimanite, which are never in mutual contact, is consistent with the breakdown of the assemblage gedrite + sillimanite + quartz into cordierite via the continuous Fe–Mg reaction



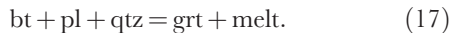
The presence of staurolite associated with cordierite suggests the reaction



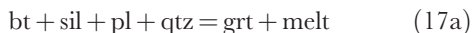
## Pelitic migmatite

### *Prograde biotite dehydration melting*

Partial melting is suggested by field relationships and by the observation of residual inclusions of biotite, plagioclase, and quartz in phases such as garnet or spinel, interpreted as incongruent phases. In the silica-saturated layer (layer A, Fig. 6), the occurrence of biotite, plagioclase and quartz included in garnet suggests that melting occurred probably via the multivariant biotite dehydration melting reaction

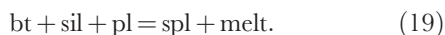


Sillimanite was not observed; however, we suggest that this silica-saturated layer could have experienced partial melting by the reaction



up to exhaustion of sillimanite. Because of the large modal proportion of garnet in this layer in comparison with leucosome, we speculate that a significant amount of melt was removed.

In the quartz-absent layer (layer B, Fig. 6), spinel and garnet have inclusions of rounded biotite, plagioclase and sillimanite, which are never in mutual contact. Although quartz has not been observed as an inclusion in garnet, melting in layer B may have occurred initially through the biotite dehydration melting reaction (17a). In a silica-poor protolith (layer B), quartz would be rapidly exhausted by reaction (17a) and consequently melting would occur through the following quartz-absent biotite dehydration reactions:



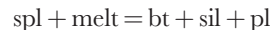
Spinel produced by biotite dehydration melting is typically associated with ilmenite–corundum intergrowth. In equivalent metapelite granulites, Sengupta *et al.* (1999) interpreted similar aggregates as the breakdown products of a former Ti-rich spinel, itself produced by the melting of Ti-rich biotite through the reaction



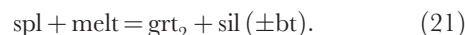
### *Partial back melting reactions and late chemical re-equilibration*

A sequence of retrograde reactions affected the peak metamorphic assemblage, particularly in the silica-undersaturated layer (B). In the silica-saturated layer (A), the *in situ* crystallization of a small proportion of melt

released volatile components involved in the late crystallization of hydrous minerals, such as biotite in association with plagioclase and quartz. In the silica-undersaturated layer (B), incongruent phases such as spinel are partially replaced by sillimanite and biotite consistent with the partial back reaction between crystallizing melt and restite (Kriegsman, 2001) via the reaction



which corresponds to the reversal of reaction (19). The local crystallization of small euhedral garnet (grt<sub>2</sub>) and the retrograde stable assemblage garnet–sillimanite–biotite are interpreted as the products of the back melting reaction (Kriegsman & Hensen, 1998)



The occurrence of a spinel- or corundum-bearing restitic layer (B) in contact with a quartzofeldspathic leucosome (D), representing *in situ* crystallizing melt, implies chemical disequilibrium on a millimetre scale at peak metamorphic conditions. Local chemical equilibration between the melt and the residuum was achieved by crystallization of the monomineralic sillimanite-rich layer (layer C) at the interface of both domains during cooling.

## *P–T* EVOLUTION

### **Mg-granulites: a continuous and complex petrographic path**

#### *Thermobarometric estimates*

Temperatures of stages 1 and 2 have been estimated using the grt–opx Al-solubility-based thermometer, corrected for late Fe–Mg exchange, of Pattison *et al.* (2003) (Table 9). The lack of plagioclase in our assemblages requires inputting the pressure as a known variable in the program RCLC-P of Pattison *et al.* (2003). Independent pressures have been calculated with the semi-empirical grt–opx Al-barometer of Harley & Green (1982), which appears to be less sensitive to late Fe–Mg exchange (Fitzsimons & Harley, 1994; Pattison & Bégin, 1994; Harley, 1998a). Peak metamorphic conditions of stage 1, calculated using garnet porphyroblast (grt<sub>1</sub>) or the garnet exsolution lamellae combined with the orthopyroxene porphyroblasts (opx<sub>2</sub>) vary from 960 ± 10°C to 1040 ± 10°C and 10.3 ± 0.5 kbar to 11.2 ± 0.1 kbar (Table 9). Average *P–T* conditions are 1000 ± 50°C, 10.5 ± 1 kbar. The temperature and pressure of the second stage (stage 2) have been estimated using the composition of the garnet rim (grt<sub>1</sub>) in direct contact with orthopyroxene (opx<sub>2</sub>) associated with cordierite (crd<sub>2</sub>), or sapphirine (spr<sub>2</sub>)–spinel (spl<sub>2</sub>) formed at the expense of the garnet. A reference pressure of 7 kbar was used, which corresponds to the typical minimal

Table 9: Summary of thermobarometric estimates for the Mg-granulites

Sample	<i>n</i>	X <sub>Mg</sub> grt cor	X <sub>Mg</sub> grt uncor	X <sub>Al</sub> opx	X <sub>Mg</sub> opx cor	X <sub>Mg</sub> opx uncor	<i>P</i> ref. (kbar)	P&al. 03 (°C)	<i>T</i> ref. (°C)	H&G 82 (kbar)
<b>Stage 1 (peak UHT metamorphism)</b>										
<i>grt<sub>1</sub> included in opx<sub>1</sub> (core)</i>										
C43	4	0.58–0.60	0.54–0.55	0.18–0.19	0.71–0.72	0.76–0.77	11	1030 ± 20	1050	11.4 ± 0.2
<i>grt<sub>1</sub> and opx<sub>1</sub> (high-Al content)</i>										
C43	10	0.60–0.62	0.54–0.56	0.15–0.19	0.73–0.75	0.76–0.79	11	1000 ± 20	1000	9.8 ± 0.4
C38	4	0.55–0.57	0.52–0.56	0.16–0.17	0.70–0.72	0.73–0.74	11	990 ± 20	1000	10.3 ± 0.4
A4-5	6	0.55–0.56	0.51–0.52	0.19	0.70–0.71	0.74–0.76	11	930 ± 10	950	10.7 ± 0.1
A4-11	2	0.55–0.57	0.49–0.52	0.16	0.70–0.71	0.74	11	970 ± 10	1000	11.0 ± 0.2
								960 ± 10		10.7 ± 0.1
<i>grt<sub>1</sub> cores and opx<sub>1</sub> (low-Al core)</i>										
A4-5	6	0.55–0.56	0.51–0.52	0.14	0.68–0.69	0.73–0.74	11	1040 ± 10	1050	11.2 ± 0.1
<i>grt exsolution and opx<sub>1</sub> (core)</i>										
C43	2	0.57–0.60	0.48–0.51	0.17–0.19	0.71–0.73	0.76–0.78	11	1025 ± 10	1000	9.7 ± 0.1
A4-5	6	0.53–0.55	0.48–0.49	0.14–0.17	0.67–0.69	0.74–0.76	11	980 ± 40	1000	11.5 ± 0.9
A4-11	1	0.55	0.46	0.16	0.69	0.74	11	975	1000	10.9
								1000 ± 10		10.3 ± 0.5
<b>Stage 2 (UHT–ITD)</b>										
<i>grt<sub>1</sub> (rim) and opx<sub>2</sub> (symplectites)</i>										
C43	5	0.59–0.64	0.56–0.57	0.15–0.17	0.78–79	0.80–0.81	7	840 ± 30	850	6.5 ± 0.4
C38	4	0.55–0.57	0.49–0.54	0.16–0.17	0.70–0.71	0.73–0.75	7	880 ± 20	900	7.3 ± 0.3
A4-5	8	0.57–0.59	0.50–0.52	0.15–0.18	0.72–0.74	0.75–0.78	7	870 ± 30	900	7.6 ± 0.5
A4-11	4	0.56–0.59	0.46–0.50	0.14–0.17	0.74–0.75	0.75–0.77	7	830 ± 20	850	8.5 ± 0.5
								860 ± 20		7.4 ± 0.2

*n*, number of garnet–orthopyroxene pairs; P&al. 03, Pattison *et al.* (2003); H&G 82, Harley & Green (1982).

pressure estimates for reactions involving garnet breakdown into orthopyroxene-bearing symplectites (Harley *et al.*, 1990; Bertrand *et al.*, 1992; Kriegsman & Schumacher, 1999). Average temperatures are in the range of 840–870°C. Because 7 kbar is a minimum pressure, temperature estimates for this second stage must be considered as minimum estimates. Independent pressures calculated at 850–900°C are in a range of 6.5 ± 0.4 to 8.5 ± 0.5 kbar. The average *P–T* conditions of the retrograde stage, corresponding to the breakdown of peak metamorphic garnet, are 900 ± 50°C, 7.5 ± 1 kbar.

#### *FMASH petrogenetic grid and role of fluids*

*Perple\_X'03* (Connolly, 1990) has been used for the calculation of the petrogenetic grid in the FMASH system (Fig. 9a) using the 2002 revised version of the internally consistent thermodynamic dataset of Holland & Powell (1998) (*Perple\_X'03* data filename of October 2003: hp02ver.dat and newest\_format\_solut.dat). Phases and end-members used in the solid-solution models involved in this grid are: garnet (pyrope, almandine), orthopyroxene (enstatite, ferrosilite, Mg-Tschermak), spinel (spinel,

hercynite), sapphirine [sapphirine (793), Fe-sapphirine (793), sapphirine (421)], cordierite (Mg-cordierite, Fe-cordierite, Mg-hydrous cordierite), sillimanite–kyanite, quartz.

Figure 9a illustrates the stable invariant points ([spl,V], [qtz,V], [opx,V] and [sil,V]), the invariant point [qtz] and the univariant reaction (spl–spr) in the FMASH system. The topology of the grid under anhydrous conditions is consistent with those proposed by Hensen & Harley (1990) and Ouzegane *et al.* (2003). An increase in water activity has the main effect of extending the garnet–cordierite stability field to higher pressure (~4 kbar for fully hydrated conditions) at the expense of the orthopyroxene–sillimanite–quartz stability field (see arrows in Fig. 9a) (Newton, 1972; Aranovich & Berman, 1996; Ouzegane *et al.*, 2003). Graphically, this occurs by translating the invariant points [spl], [opx], [sil] and [qtz] towards higher pressure along their respective (crd) reactions. Because water activity cannot be constrained accurately, the relative position of the grid in *P–T* space remains uncertain. The petrographic *P–T* evolution is therefore interpreted using a partial and

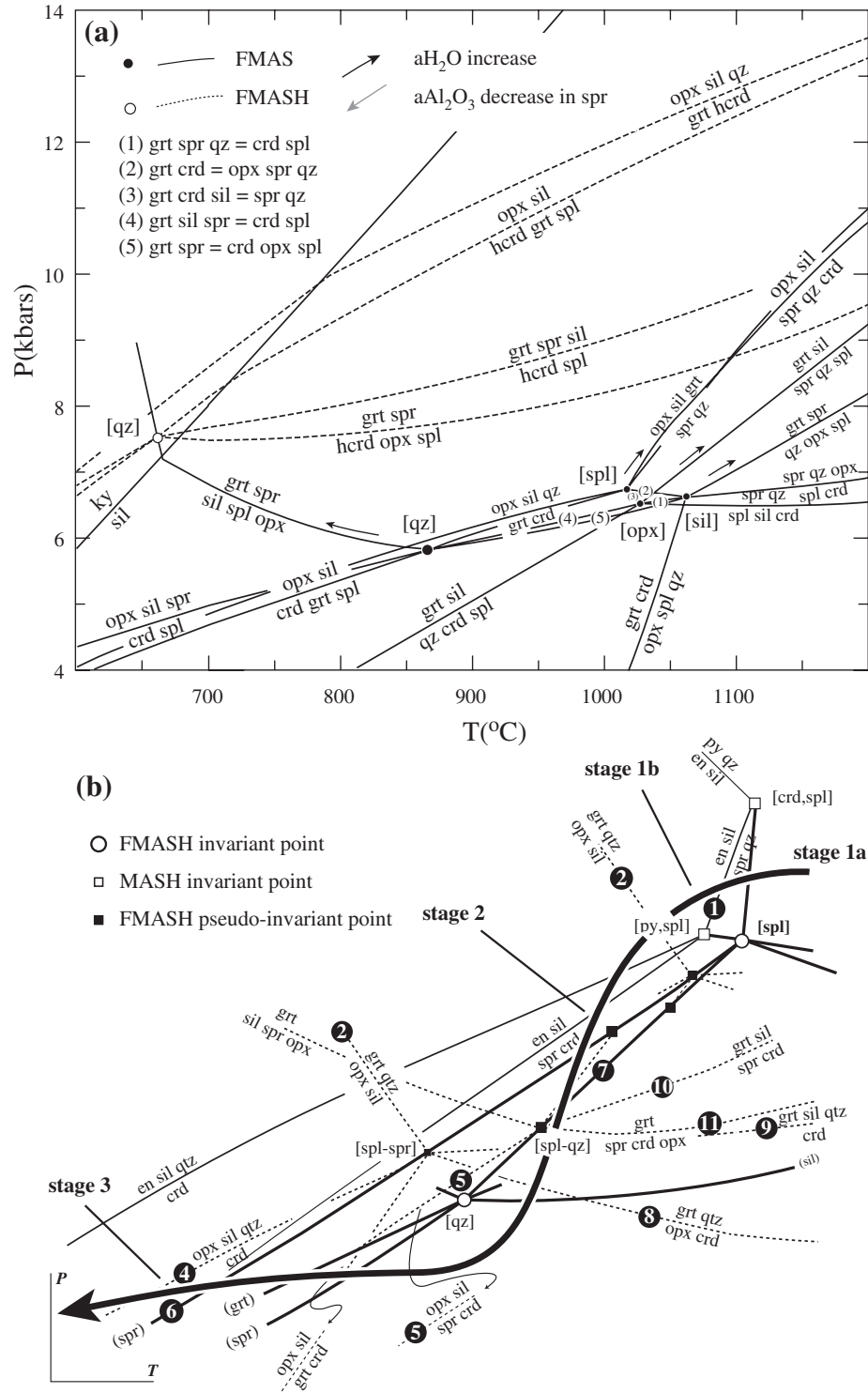


**Fig. 9.** (a) Quantitative FMAS(H) petrogenetic grids involving garnet, orthopyroxene, sapphirine, cordierite, spinel, sillimanite and quartz. This grid is constructed using a sapphirine solid solution model involving Fe–Mg and Tschermak substitution. The amount of Tschermak substitution is restricted to the range 0.85 spr7 to 1.00 spr7, which covers the natural composition of our samples. (b) Partial qualitative grid in the FMASH system showing the main univariant reactions (spl–spr), (spl–qtz) and (qtz–sil) (bold lines) used for the construction of the petrographical path. The dashed lines show the orientation of the five divariant reactions associated with the univariant reactions (spl–spr) and (spl–qtz). Such divariant reactions are the equivalent to Fe–Mg isopleths of continuous reactions. The thin lines correspond to selected MAS univariant reactions related to the invariant point [py–spl] and [crd,spl]. Numbers in circles refer to continuous and discontinuous reactions given in the text.

semi-quantitative grid in the FMASH system (Fig. 9b). The  $P$ - $T$  evolution inferred from textural relations and geothermobarometry can be divided into three stages and is illustrated in Fig. 9b.

(1) The peak metamorphic assemblage (stage 1a) sapphirine-garnet-quartz + orthopyroxene or sillimanite suggesting ultrahigh-temperature conditions  $>1050^{\circ}\text{C}$  (Chatterjee & Schreyer, 1972; Newton, 1972; Bertrand *et al.*, 1991) is destabilized through the reactions  $\text{spr}_{1a} + \text{qtz} = \text{opx}_{1b} + \text{sil}_{1b}$  (1) and  $\text{grt}_{1a} + \text{qtz} = \text{opx}_{1b} + \text{sil}_{1b}$  (2), which indicate cooling at a pressure above the FMASH invariant point [spl].

(2) Subsequent to this high-grade event at relatively high pressure, a near-isothermal decompression (stage 2) is inferred with high confidence from the succession and orientation of numerous secondary continuous reactions (Fig. 9b). The univariant reaction  $\text{opx}_{1b} + \text{sil}_{1b} = \text{grt}_2 + \text{spr}_2 + \text{crd}_2$  (7) and the numerous associated divariant reactions [(4)–(6), (8)–(12)] imply a temperature during decompression between the invariant points [spl] and [qtz] (Fig. 9b) of about  $850$ – $900^{\circ}\text{C}$  according to our thermobarometric estimates of stage 2 (Table 9). The Al content of orthopyroxene ( $\text{opx}_2$ ) produced during the decompression is constant and of the same order as that of the porphyroblast ( $\text{opx}_1$ ) (about 7–8 wt %). Because Al isopleths in a  $P$ - $T$  space are mostly temperature independent (Aranovich & Berman, 1996), this suggests that the decompression was nearly isothermal. Finally,  $\text{grt}_1$  breakdown into  $\text{opx}_2$ - $\text{crd}_2$ - $\text{spl}_2$  (12) suggests that the univariant reaction garnet + sapphirine = cordierite + orthopyroxene + spinel (qtz-sil) was crossed during decompression (Fig. 9b). Because this reaction is mostly pressure independent (Fig. 9b), this indicates that isothermal decompression proceeded to pressures lower than the invariant point [qtz] (about 7 kbar according to the barometric estimates). To conclude, stage 2 corresponds to a near-isothermal decompression (ITD) at ultrahigh-temperature conditions ( $850$ – $950^{\circ}\text{C}$ ) of  $\sim 4$  kbar.

(3) The final stage (stage 3) involves breakdown of cordierite ( $\text{crd}_2$ ), into a new  $\text{opx}_3$ - $\text{sil}_3 \pm \text{qtz}$  assemblage. According to the positive  $dP/dT$  slopes of the divariant reactions cordierite = orthopyroxene + sillimanite + quartz and cordierite + sapphirine = orthopyroxene + sillimanite [respectively reactions (4) and (5) in Fig. 9b], an isobaric cooling (IBC) at a pressure below the invariant point [qtz] (about 7 kbar), may explain the new orthopyroxene-sillimanite-quartz assemblage (Fig. 9b). The distinctly lower Al content of the newly formed orthopyroxene ( $\text{opx}_3$ ) ( $\sim 4$  wt %) in comparison with  $\text{opx}_{0-1}$  and  $\text{opx}_2$  implies that they crystallized at lower temperatures ( $\sim 700$ – $800^{\circ}\text{C}$ ). Orthoamphibole-cordierite-bearing rocks (An4c and A6-3) provide additional information on stage 3 of the  $P$ - $T$  evolution. It is noteworthy that despite the extensive hydration, the preservation of residual orthopyroxene with garnet

exsolution lamellae suggests that these rocks have also been subjected to UHT metamorphic conditions. Textures and assemblages are interpreted using a semi-quantitative FMASH grid involving gedrite, staurolite, garnet, orthopyroxene, cordierite, sillimanite, kyanite, and quartz under fully hydrated conditions (Fig. 10a and b). Location of the FMASH divariant reactions (14), (15) and (16) is consistent with a shallow  $dP/dT$  path at pressures between 5 and 8 kbar (Fig. 10b).  $P$ - $T$  conditions estimated for these orthoamphibole-bearing rocks are 4.5–5.5 kbar and  $600$ – $650^{\circ}\text{C}$  (Nicollet, 1988). In conclusion, the final stage 3 recorded by the Mg-granulites is interpreted as a cooling from  $\sim 7$  kbar,  $850^{\circ}\text{C}$  to  $\sim 5$  kbar,  $650^{\circ}\text{C}$ .

### Metapelitic migmatites: heating-cooling path

Determining accurate metamorphic conditions for the pelitic migmatite C61 is strongly limited by the lack of cordierite or orthopyroxene, and by the lack of large-scale equilibrium. Therefore,  $P$ - $T$  conditions are basically approached using a petrogenetic grid in the KFMASH system including the ‘haplogranite’ model of Holland & Powell (1998) and White *et al.* (2001). An attempt at barometric estimates of the peak metamorphism yields a mean pressure of about 7–8 kbar using the calibration of Hodges & Crowley (1985) and Koziol & Newton (1988) of the garnet-plagioclase-sillimanite-quartz barometer (GASP) and assuming a peak temperature of  $850^{\circ}\text{C}$  (temperature was inferred from the petrogenetic grid; see section below).

#### KFMASH petrogenetic grid

The grid calculated with *Perple\_X'03* shows univariant reactions and also the location of some pseudo-divariant reactions in the KFMASH system. The topology of the proposed grid is very similar to that of the White *et al.* (2001) grid except that we do not assume quartz as an excess phase to interpret the silica-undersaturated assemblage within the pelitic migmatite C61. Consequently, in addition to the four [x, $\mu$ , $\text{H}_2\text{O}$ ] stable invariant points of the White *et al.* (2001) grid (i.e. [spl], [bt], [opx] and [sil]), the invariant point [qtz] is also stable (Fig. 11). The low-temperature side of the grid involving muscovite and the  $\text{H}_2\text{O}$ -absent reactions is not represented for clarity.

In the silica-saturated layer (A), partial melting occurred through the breakdown of biotite + plagioclase + quartz  $\pm$  sillimanite to garnet and melt. In the KFMASH grid (Fig. 11), this reaction, (17a), is restricted to the low-temperature side of the univariant reaction (opx-spl) and is experimentally constrained at  $850$ – $875^{\circ}\text{C}$  using an average metapelitic composition (Vielzeuf & Holloway, 1988; Gardien *et al.*, 1995). Pressure cannot be constrained

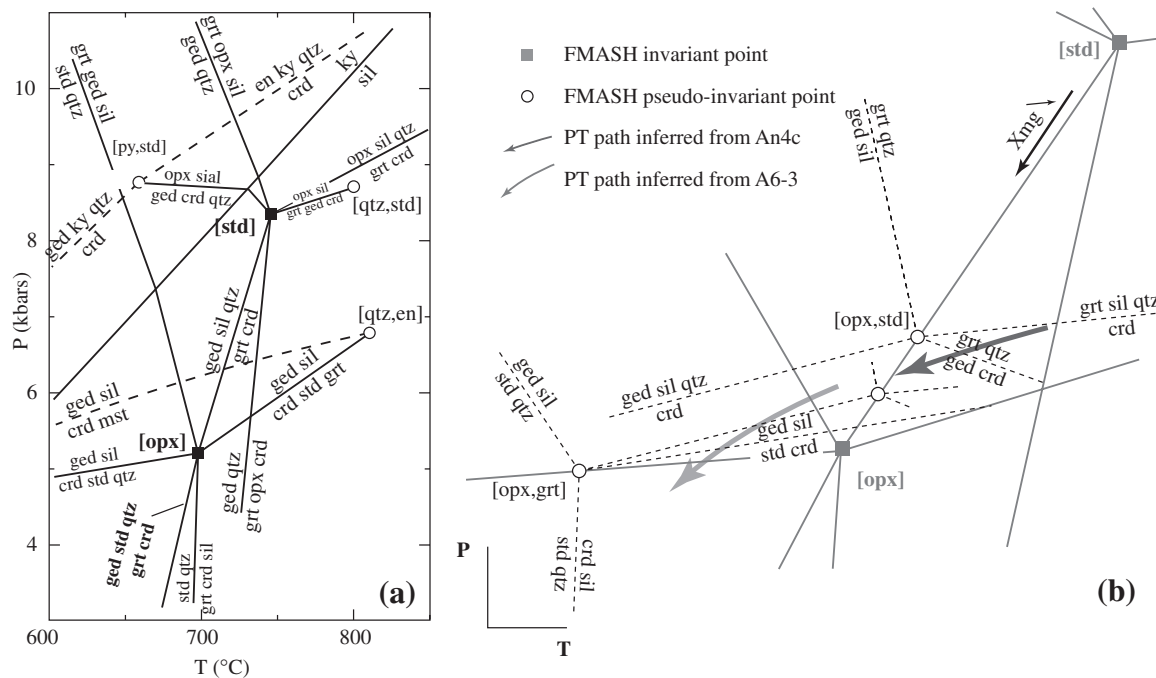


**Fig. 10.** (a) Semi-quantitative FMASH petrogenetic grid involving quartz, garnet, orthopyroxene, cordierite, staurolite, gedrite, kyanite and sillimanite under pure  $H_2O$  conditions [modified after Harley (1985)].  $P$ - $T$  position of the MASH invariant points (○) and three main MASH univariant reactions (dashed lines) have been quantified with the thermodynamic data of Holland & Powell (1998) using the *Perple\_X'03* software of Connolly (1990). FMASH invariant points (■) and univariant curves (continuous lines) have been qualitatively positioned according to topological constraints. (b) Partial FMASH qualitative grid showing the divariant reactions (dashed lines), associated with the univariant reactions (opx–std) and (opx–grt) (grey continuous lines), used to constrain the  $P$ - $T$  petrographic path of samples An4c and A6-3.

precisely, as the melting reaction (17a) is stable over a wide range of pressure, from 5 to ~15 kbar at about 850°C (Vielzeuf & Schmidt, 2001). The peak metamorphic assemblage of the silica-undersaturated layer (B) is characterized by the coexistence of garnet, spinel, biotite, sillimanite and melt produced by the multivariant reactions (18) and (19). The stability field of this assemblage occurs in the low-temperature side of the KFMASH grid at temperatures below the univariant reaction (opx–crd), (opx–qtz) and (qtz–crd). Consequently, maximum temperatures did not exceed 830°C at 5 kbar and 910°C at 7 kbar. Thus, it appears that peak metamorphic conditions inferred from both assemblages (layers A and B) are in good agreement. By combining the thermobarometric estimates and petrogenetic grid evidence, peak metamorphism may be constrained at ~850–870°C, ~7–8 kbar.

The retrograde evolution is mainly characterized by the development of biotite + sillimanite ± garnet produced by the reverse of reaction (19) and reaction (21). No textures of decompression, such as the garnet + sillimanite breakdown to spinel + cordierite symplectites, commonly interpreted as a result of decompression have been observed. This suggests that cooling occurred without significant decompression at about 7 kbar (Fig. 11).

### Summary of $P$ - $T$ evolution

Petrogenetic data derived from a suite of lenses of Mg-granulite located within the migmatitic basement are summarized in Fig. 12. This shows that each rock type experienced distinct petrographical  $P$ - $T$  evolutions. The Mg-granulites are characterized by an apparently continuous and complex  $P$ - $T$  path that has been subdivided into three distinct stages. Peak metamorphic conditions at ultrahigh-temperature conditions ( $1000 \pm 50^\circ\text{C}$  and  $10.5 \pm 1.5$  kbar; stage 1) were followed by a near-isothermal decompression (ITD) of about 3–4 kbar at 900–950°C (stage 2). Finally, stage 3 corresponds to near IBC associated with variable hydration at 6–7 kbar from 900 to 650°C. The host pelitic migmatite does not record evidence of UHT conditions and ITD. Partial melting occurred at peak metamorphic conditions of about 850°C, 7 kbar, following a simple heating-cooling path without significant change in pressure (Fig. 12). The retrograde  $P$ - $T$  path of the migmatite is similar to the final part (stage 3) of the  $P$ - $T$  path of the Mg-granulites (Fig. 12). The migmatite and tonalitic host gneisses lack evidence of UHT metamorphism probably for two reasons. First, they lack the appropriate bulk composition (i.e. a highly aluminous and magnesian composition) to

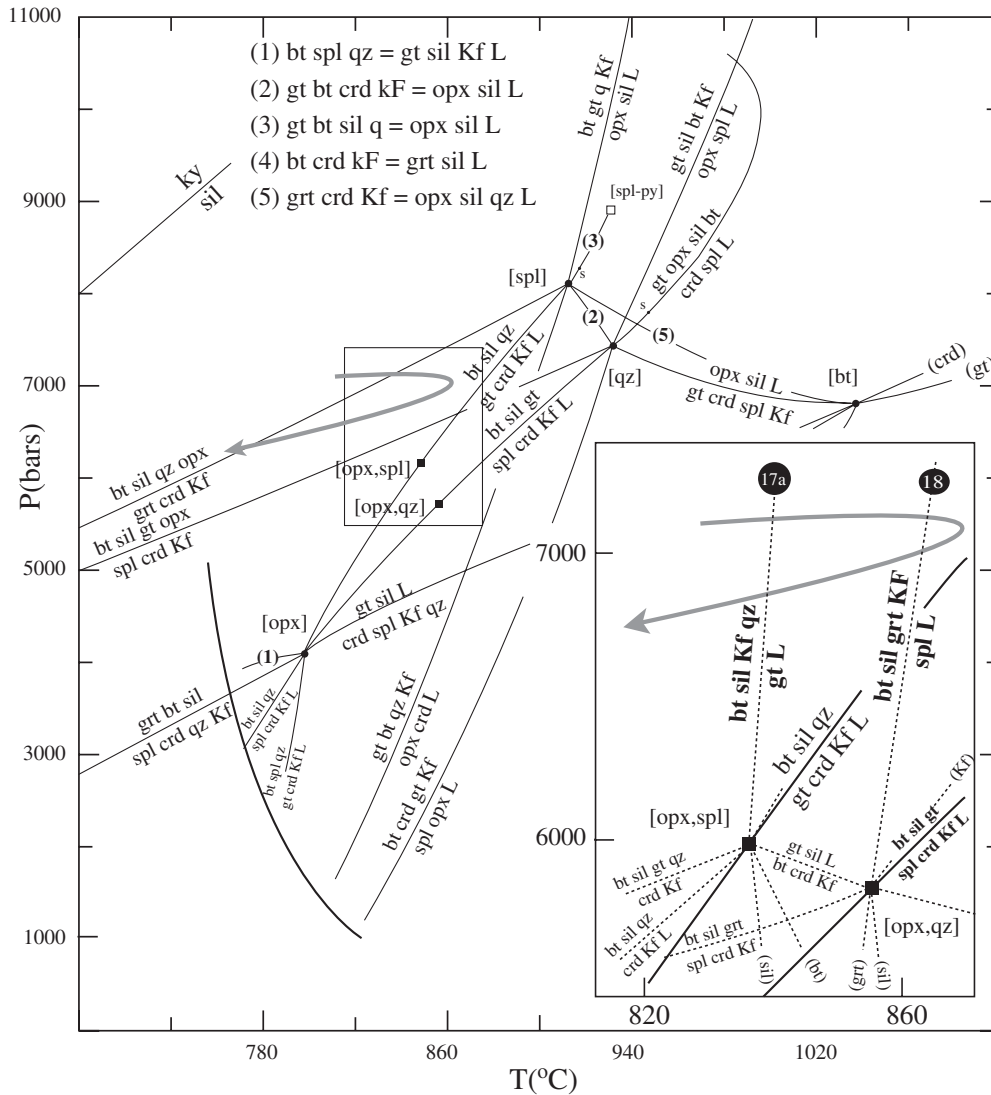


**Fig. 11.** Quantitative petrogenetic grid in the KFMASH system for fluid-absent metapelite involving garnet, cordierite, biotite, orthopyroxene, spinel, sillimanite, K-feldspar, quartz and melt (L) modified from White *et al.* (2001). Bold lines and black points (●) correspond to the univariant lines and invariant points in the KFMASH system. Dashed lines show the topology of the pseudo-univariant reactions associated with the pseudo-invariant points (opx–spl) and (opx–qtz) (■). The *P–T* location of these pseudo-invariant points is arbitrary. The arrows correspond to the *P–T* path inferred for the pelitic migmatite C61.

form UHT assemblages. Second, any assemblages that may have formed were obliterated by later melting and subsequent hydration that occurred during freezing of those melts.

**CHEMICAL U–Th–Pb DATING**

To determine the tectonic implications of these different *P–T* paths, it is essential to constrain the timing. This is particularly crucial in north-central Madagascar and Andriamena where three distinct magmatic and metamorphic events are recognized: at ~2.5 Ga, 820–720 Ma and 550–500 Ma (Guérrot *et al.*, 1993; Tucker *et al.*, 1999;

Kröner *et al.*, 2000; Goncalves *et al.*, 2003). There is a strong possibility that portions of the *P–T* paths may be ascribed to distinct thermotectonic events and that the complex petrographical path of the Mg-granulites may have resulted from superposition of several events, as suggested in East Antarctica (Harley, 1998a) and India (Raith *et al.*, 1997; Rickers *et al.*, 2001).

Geochronological data were obtained using the EMP method of dating monazite (Montel *et al.*, 1996). Because of its *in situ* nature and very high spatial resolution, EMP dating permits the combination of geochronological information with metamorphic petrology to construct *P–T–t* paths.

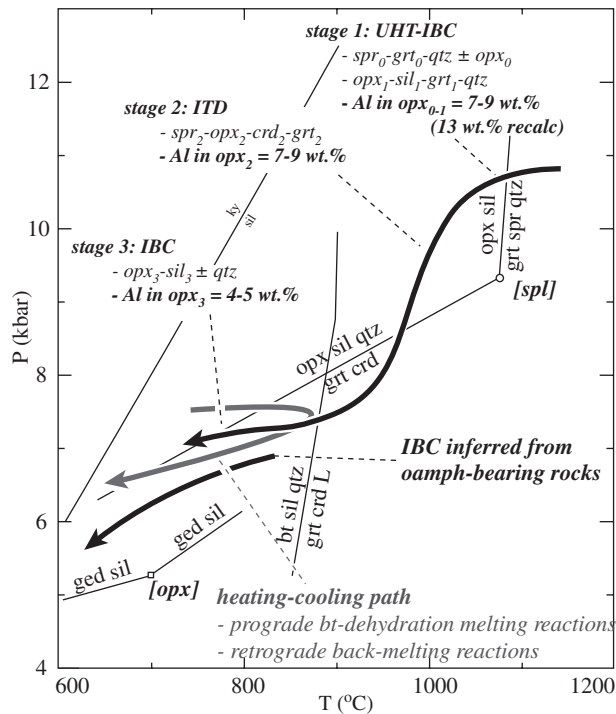


**Fig. 12.** *P*-*T* diagram summarizing the distinct petrographic *P*-*T* paths inferred from the Mg-granulites (sapphirine-bearing and orthoamphibole-bearing rocks) and the pelitic migmatite from the Andriamena unit (north-central Madagascar).

### Analytical procedure and data processing

The theoretical basis and associated statistical treatment of data follow the analytical procedure detailed by Montel *et al.* (1994, 1996). Measurements were performed on a Cameca SX100 electron microprobe at the Laboratoire Magmas et Volcans, Clermont-Ferrand. Analytical conditions include an accelerating voltage of 15 kV and a beam current of 150 nA. U and Th were analysed successively with a PET crystal on the same wavelength-dispersive spectrometer with a counting time of 225 s and 75 s on peak, respectively. Pb was analysed with an LPET crystal using a 300 s counting time on peak. P, Ca, Si and Y were analysed successively with a PET crystal on the same spectrometer with a 30 s counting time for P and Ca, and 90 s for Si and Y. Light rare earth elements (LREE; La, Ce, Pr, Nd, Sm and Gd) were analysed using an LIF crystal with counting time of 30 s for La and Ce, 45 s for Pr and Nd, and 60 s for Sm and Gd. Counting time for the background corresponds to half of peak time for each element, on both sides of the peak. X-ray lines and background offsets, which were not always symmetrical with respect to the peak, were selected to minimize the X-ray line interferences. X-ray lines selected were:  $\text{K}\alpha$  for P, Ca and Si;  $\text{L}\alpha$  for Y, La and Ce;  $\text{L}\beta$  for Pr, Nd, Sm and Gd;  $\text{M}\alpha$  for Th and Pb;  $\text{M}\beta$

for U. The Pb  $\text{M}\alpha$ -Y  $\text{L}\gamma$  overlap correction factor was 0.0018. The U  $\text{M}\beta$ -Th  $\text{M}\gamma$  overlap was not corrected.

Standards used were  $\text{UO}_2$  and  $\text{ThO}_2$  for U and Th, apatite for Ca, zircon for Si, and synthetic phosphates for the REE, P and Y ( $\text{LaPO}_4$ ,  $\text{CePO}_4$ , etc.). For Pb, a synthetic glass was used for calibration. Beam current used for standards was 100 nA. Counting time was 50 s on peak and 20 s on background for  $\text{UO}_2$  and  $\text{ThO}_2$ , and 300 s on peak and 100 s on background for PbO. Counting times for LREE and other elements (Ca, Si, P and Y) were 80 s and 40 s respectively on peak, and 20 s and 10 s respectively on background.

Errors in U, Th and Pb contents and detection limits were calculated using the procedure of Ancey *et al.* (1978). Individual ages, which are referred to as measurements, were calculated from the U, Th and Pb concentrations. The  $2\sigma$  errors given on measurements depend on U, Th and Pb contents and were calculated by propagating the uncertainties in these elements (at the 95% confidence level) into the decay equation. Sample ages and associated errors (with 95% confidence level) were calculated by averaging the individual measurements assuming that they belong to a single population. A least-squares modelling approach was applied to the whole population of measurements to identify multiple populations (Montel *et al.*, 1996). The quality of the modelling is assessed from the mean square of weighted deviates (MSWD). The whole measurement population is graphically depicted in weighted histograms, where each measurement and its uncertainty are represented by bell-shaped probability curves.

A recent study by Jercinovic & Williams (2004) has demonstrated that inaccurate background subtraction and interference correction can lead to dramatic errors of 50 Ma or more in EMP dating when concentrations approach the trace element range. Because our background was estimated via a simple two-point linear interpolation and U  $\text{M}\beta$ -Th  $\text{M}\gamma$  interference was not considered, variations below 50 Ma in chemical ages will not be over-interpreted in this study.

### U-Th-Pb dating results

Representative chemical compositions are presented in Table 10. U-Th-Pb data for the investigated samples are presented in Tables 11 and 12, and on weighted-histogram representations in Fig. 15.

#### *Mg-granulite A4-5: evidence of a peak $\text{grt}_1\text{-spr}_1\text{-qtz}$ assemblage (stage 1)*

In sample A4-5, three populations of monazite are distinguished according to their textural position and chemical composition.

Table 10: Representative chemical compositions of monazite and their formula calculated on the basis of 16 oxygens

Sample:	A4-5	A4-5	A4-5	A4-5	An4c	A4-31	C17	A6-3	C61	C61
Monazite:	M5	M1	M2	M12	M31	M4	M3	M1	M7	M21
Analysis:	incl. grt <sub>1</sub>	matrix	matrix	opx <sub>3</sub> –sil <sub>3</sub>	incl. grt <sub>1</sub>	qtz	crd <sub>2</sub>	matrix	matrix	matrix
	23	26	30	8	22	4	20	29	18	25
UO <sub>2</sub>	0.09	0.09	0.08	0.35	0.26	0.09	0.09	0.10	0.29	0.39
PbO	0.53	0.45	0.14	0.14	0.22	0.18	0.22	0.31	0.12	5.37
ThO <sub>2</sub>	4.50	5.37	4.05	2.98	8.39	5.56	6.51	8.71	0.02	0.21
CaO	0.54	0.53	0.66	0.70	1.61	0.45	0.17	1.09	0.28	0.85
P <sub>2</sub> O <sub>5</sub>	28.38	28.72	29.13	30.79	29.66	29.24	27.76	28.80	30.38	29.44
Y <sub>2</sub> O <sub>3</sub>	0.69	0.40	0.09	1.49	0.45	0.01	0.03	2.55	0.67	0.31
SiO <sub>2</sub>	0.68	0.76	0.28	0.16	0.29	0.97	1.48	1.01	0.78	0.53
La <sub>2</sub> O <sub>3</sub>	14.86	15.62	12.82	10.90	11.19	13.13	15.87	15.03	16.77	16.52
Ce <sub>2</sub> O <sub>3</sub>	27.87	27.76	25.48	21.91	26.59	26.03	28.86	25.24	31.64	30.78
Pr <sub>2</sub> O <sub>3</sub>	2.86	2.86	3.11	2.61	3.13	3.23	3.33	2.19	2.89	2.54
Nd <sub>2</sub> O <sub>3</sub>	12.39	12.54	17.20	14.29	12.40	19.11	16.07	8.12	11.27	9.69
Sm <sub>2</sub> O <sub>3</sub>	2.10	1.85	3.64	6.94	2.94	1.49	0.99	1.83	2.72	1.68
Gd <sub>2</sub> O <sub>3</sub>	1.34	1.07	0.98	5.38	1.91	0.36	0.14	3.29	1.36	0.89
Total	96.82	98.02	97.67	98.64	99.04	99.85	101.52	98.27	99.20	99.19
U	0.00	0.00	0.00	0.01	0.01	0.00	0.00	0.00	0.01	0.01
Pb	0.00	0.00	0.00	0.00	0.00	0.00	0.00	0.00	0.00	0.19
Th	0.17	0.20	0.15	0.11	0.30	0.20	0.24	0.32	0.00	0.00
Ca	0.09	0.09	0.11	0.12	0.27	0.08	0.03	0.19	0.05	0.14
P	3.92	3.92	3.98	4.10	3.98	3.92	3.73	3.89	4.00	3.95
Y	0.06	0.03	0.01	0.13	0.04	0.00	0.00	0.22	0.06	0.03
Si	0.11	0.12	0.04	0.03	0.05	0.15	0.23	0.16	0.12	0.08
La	0.89	0.93	0.76	0.63	0.66	0.77	0.93	0.88	0.96	0.97
Ce	1.66	1.64	1.51	1.26	1.54	1.51	1.68	1.47	1.80	1.79
Pr	0.17	0.17	0.18	0.15	0.18	0.19	0.19	0.13	0.16	0.15
Nd	0.72	0.72	0.99	0.80	0.70	1.08	0.91	0.46	0.63	0.55
Sm	0.12	0.10	0.20	0.38	0.16	0.08	0.05	0.10	0.15	0.09
Gd	0.07	0.06	0.05	0.28	0.10	0.02	0.01	0.17	0.07	0.05
Age (Ma)	2420 ± 114	1786 ± 82	771 ± 64	759 ± 63	2505 ± 85	733 ± 49	743 ± 43	800 ± 36	521 ± 118	740 ± 42

(1) Monazite occurs as irregular grains enclosed in UHT garnet (grt<sub>1</sub>) and orthopyroxene (opx<sub>1</sub>), usually associated with apatite. Garnet and orthopyroxene display numerous cracks, which connect the monazite with the matrix (Fig. 13a). These monazites are homogeneous. They are characterized by the highest amount of ThO<sub>2</sub> (3.8–4.5 wt %), SiO<sub>2</sub> (up to 1.1 wt %) and LREE (La, Ce). Distribution patterns of matrix monazites normalized to monazite included in garnet (Fig. 14a and b) allow us to easily show the main composition features of monazite included in UHT phases compared with matrix monazite.

(2) Matrix monazite occurs as ~50–80 μm irregular grains located in the aggregates of cordierite,

orthopyroxene and sapphirine (crd<sub>2</sub>–opx<sub>2</sub>–spr<sub>2</sub>) (Fig. 13b). They are characterized by very homogeneous ThO<sub>2</sub> contents (3.9–4.1 wt %), but highly variable UO<sub>2</sub> contents (Fig. 14a). The main feature is the very low Y contents (<0.2 wt %) (Fig. 14a–c). These monazites are slightly depleted in LREE (La and Ce) and significantly enriched in Nd and Sm with respect to monazite included in UHT phases (grt<sub>1</sub> and opx<sub>1</sub>).

(3) The third population corresponds to small matrix monazites (<20 μm), which occur systematically in close association with the opx<sub>3</sub>–sil<sub>3</sub> symplectite (Fig. 13c and d). Needles of sillimanite (sil<sub>3</sub>) are partly enclosed in the monazite, suggesting that the crystallization of such monazite is syn- to post-sillimanite growth (Fig. 13d). These

Table 11: U–Th–Pb electron microprobe analyses and calculated individual ages from Mg-granulites A4-5 and An4c

mnz	Analysis	Th (ppm)	U (ppm)	Pb (ppm)	<i>T</i> (Ma)
<i>Sample A4-5</i>					
M7	1 g	61890 ± 643	1080 ± 162	5886 ± 128	1917 ± 74
	2 g	49810 ± 590	860 ± 161	4774 ± 113	1932 ± 84
	3 g	50430 ± 594	830 ± 161	4136 ± 105	1672 ± 75
M8	4 g	36110 ± 526	1290 ± 161	1496 ± 77	815 ± 62
M4	23 g	39500 ± 539	820 ± 159	4870 ± 115	2414 ± 114
	24 g	33130 ± 509	620 ± 160	1843 ± 77	1143 ± 80
M1	26 m	47220 ± 576	800 ± 161	4154 ± 105	1784 ± 82
	27 m	43240 ± 558	790 ± 160	3671 ± 100	1718 ± 85
	28 m	34650 ± 515	600 ± 156	1625 ± 77	973 ± 72
M6	22 m	26700 ± 474	2360 ± 166	1225 ± 75	780 ± 69
M2	29 m	36620 ± 526	360 ± 157	1247 ± 74	729 ± 62
	30 m	35080 ± 518	710 ± 159	1199 ± 74	708 ± 62
	31 m	35400 ± 519	1180 ± 160	1437 ± 77	805 ± 63
	32 m	35560 ± 521	760 ± 161	1329 ± 76	771 ± 64
M3	33 m	33830 ± 511	1700 ± 162	1405 ± 76	784 ± 62
	34 m	35540 ± 520	580 ± 157	1248 ± 74	736 ± 63
	35 m	35020 ± 516	590 ± 160	1278 ± 75	762 ± 65
M9	5 m	40190 ± 544	1040 ± 160	1357 ± 74	688 ± 53
M11	6 s	27580 ± 478	2130 ± 165	1315 ± 74	834 ± 70
M10	7 s	29380 ± 490	2380 ± 168	1461 ± 76	859 ± 67
M12	8 s	26210 ± 472	3190 ± 171	1249 ± 73	747 ± 63
	9 s	29040 ± 487	2800 ± 169	1193 ± 72	698 ± 59
M14	19 s	33310 ± 511	570 ± 159	1218 ± 74	763 ± 68
	20 s	32770 ± 506	1580 ± 161	1436 ± 77	831 ± 66
<i>Sample An4c</i>					
M1	36 g	54510 ± 606	720 ± 157	6098 ± 129	2265 ± 89
	37 g	64490 ± 650	1170 ± 160	6349 ± 132	1975 ± 72
M2	38 g	57140 ± 617	640 ± 161	6905 ± 139	2440 ± 94
M7	52 g	27360 ± 472	510 ± 159	2514 ± 85	1848 ± 123
	53 g	32530 ± 501	1410 ± 160	2997 ± 90	1715 ± 95
M18	1' g	49250 ± 587	1490 ± 163	4680 ± 111	1837 ± 78
M19	3' g	52600 ± 602	920 ± 161	6534 ± 134	2459 ± 97
M20	4' g	49820 ± 590	920 ± 161	6303 ± 131	2492 ± 101
M21	5' g	54970 ± 611	990 ± 162	7154 ± 143	2562 ± 98
M22	6' g	48130 ± 582	980 ± 160	6148 ± 129	2497 ± 102
M23	8' g	48890 ± 584	1570 ± 164	6644 ± 136	2541 ± 99
	9' g	51970 ± 601	1410 ± 163	6894 ± 139	2527 ± 96
M15	13' g	58650 ± 627	810 ± 161	5948 ± 127	2062 ± 80
	14' g	57960 ± 624	940 ± 161	5539 ± 121	1933 ± 76
	15' g	59590 ± 630	890 ± 160	6599 ± 135	2230 ± 84
M29	20' g	66420 ± 658	1040 ± 162	8269 ± 158	2479 ± 86
M31	21' g	55020 ± 612	2720 ± 168	7015 ± 141	2272 ± 81
	22' g	53450 ± 603	3420 ± 169	7950 ± 154	2499 ± 84

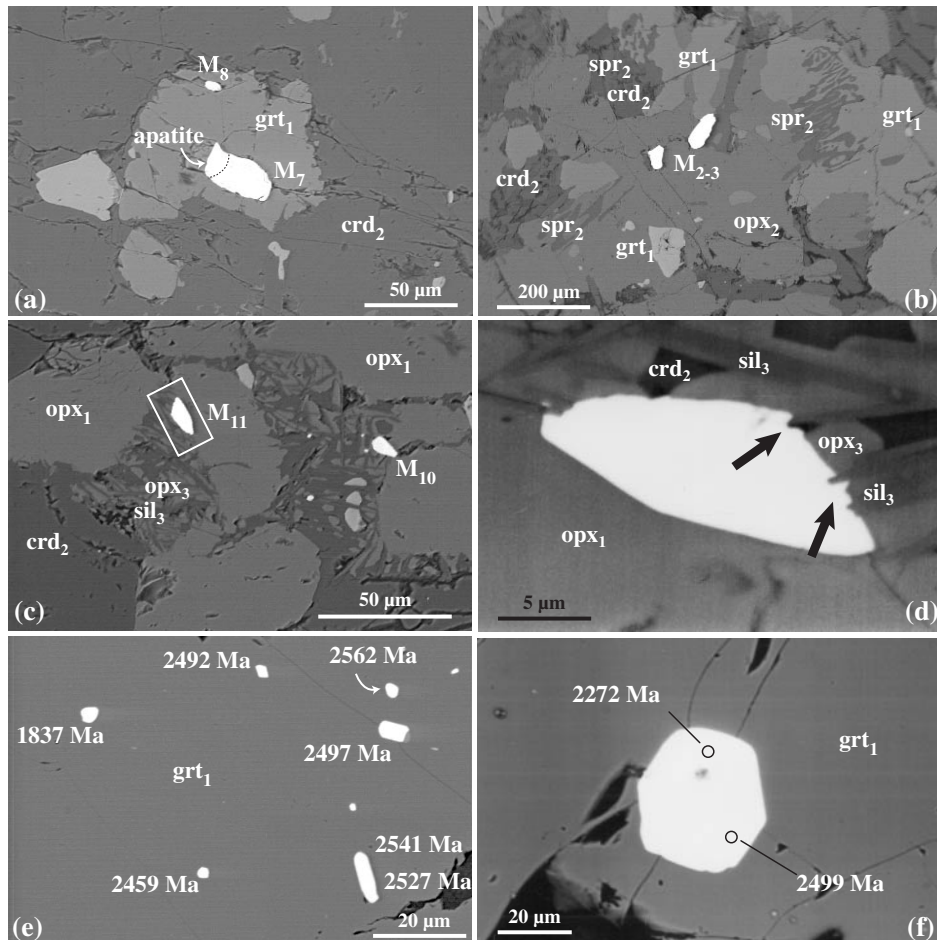
Errors at 2σ. g, monazite included in garnet; m, monazite located in the matrix; s, monazite associated with the symplectite opx<sub>3</sub>–sil<sub>3</sub>.

Table 12: U–Th–Pb electron microprobe analyses and calculated individual ages from Mg-granulites A4-31, C17 and A6-3 and the pelitic migmatite C61

mnz	Analysis	Th (ppm)	U (ppm)	Pb (ppm)	T (Ma)	mnz	Analysis	Th (ppm)	U (ppm)	Pb (ppm)	T (Ma)
<i>Sample A4-31</i>						<i>Sample A6-3</i>					
M1	1	35380 ± 519	610 ± 158	1180 ± 74	697 ± 62	M1	28	78070 ± 706	1050 ± 162	2953 ± 91	798 ± 36
M2	2	39100 ± 538	590 ± 159	1320 ± 76	711 ± 58		29	76550 ± 702	880 ± 163	2844 ± 90	790 ± 36
M3	3	34640 ± 515	950 ± 161	1277 ± 76	747 ± 64		30	79980 ± 710	980 ± 162	2868 ± 90	761 ± 34
M4	4	48830 ± 588	830 ± 160	1710 ± 80	733 ± 49		31	75910 ± 697	890 ± 162	2872 ± 91	803 ± 37
M5	5	52430 ± 604	770 ± 160	1830 ± 81	735 ± 46		32	73880 ± 690	840 ± 162	2826 ± 91	813 ± 38
M6	6	34260 ± 511	340 ± 157	1120 ± 74	700 ± 66		33	77320 ± 705	820 ± 163	2970 ± 92	818 ± 37
	7	39190 ± 538	610 ± 160	1300 ± 75	697 ± 57		34	81280 ± 717	830 ± 162	2148 ± 83	568 ± 30
M7	8	48510 ± 585	620 ± 161	1750 ± 79	764 ± 50	M4	29'	99160 ± 782	1270 ± 164	3572 ± 99	763 ± 30
M8	9	36680 ± 532	1090 ± 164	1406 ± 76	771 ± 60		30'	108460 ± 814	1320 ± 166	4003 ± 104	783 ± 29
	10	36230 ± 527	1170 ± 162	1396 ± 76	770 ± 61		32'	64510 ± 649	1020 ± 160	2360 ± 85	767 ± 40
<i>Sample C17</i>						M5	33'	71260 ± 679	970 ± 162	2581 ± 87	765 ± 37
M1	1	30830 ± 503	750 ± 163	1154 ± 73	764 ± 71		34'	86500 ± 736	1210 ± 163	2340 ± 85	573 ± 28
	2	30400 ± 498	710 ± 163	1055 ± 72	712 ± 70		35'	72510 ± 686	820 ± 162	2689 ± 88	789 ± 38
	3	35630 ± 529	530 ± 162	1219 ± 72	721 ± 62		36'	79890 ± 712	940 ± 162	2220 ± 84	593 ± 31
M2	4	28450 ± 493	430 ± 166	989 ± 71	731 ± 77	M6	37'	72260 ± 683	930 ± 162	2635 ± 88	772 ± 37
	5	29160 ± 494	250 ± 164	970 ± 72	716 ± 76		38'	71220 ± 679	1060 ± 161	2695 ± 89	795 ± 38
	6	30830 ± 504	360 ± 164	990 ± 71	684 ± 70		39'	69690 ± 673	930 ± 162	2731 ± 88	827 ± 40
	7	34100 ± 525	730 ± 165	1198 ± 73	725 ± 64	M2	40'	69340 ± 670	920 ± 160	2552 ± 87	778 ± 38
	8	60020 ± 648	670 ± 166	2100 ± 81	745 ± 42		41'	66600 ± 659	900 ± 162	2530 ± 86	802 ± 40
	9	76000 ± 709	990 ± 168	2700 ± 87	752 ± 35		42'	64390 ± 651	1570 ± 162	2558 ± 87	810 ± 40
	10	65250 ± 668	640 ± 166	2370 ± 84	777 ± 40		43'	65540 ± 654	1100 ± 160	2400 ± 85	765 ± 39
	11	56770 ± 630	610 ± 164	2040 ± 80	766 ± 44	<i>Sample C61</i>					
	12	40580 ± 556	400 ± 165	1350 ± 74	713 ± 57	M1	15	27000 ± 476	8720 ± 188	1838 ± 118	722 ± 41
	13	41240 ± 560	490 ± 164	1320 ± 74	681 ± 54	M10	14'	30290 ± 498	6290 ± 181	1747 ± 122	750 ± 46
	14	68130 ± 680	650 ± 166	2320 ± 84	730 ± 38		21'	42830 ± 566	3690 ± 175	1805 ± 120	723 ± 43
	24	46760 ± 584	500 ± 162	1730 ± 77	788 ± 52	M11	3'	25310 ± 468	6690 ± 183	1587 ± 120	734 ± 48
M3	15	40510 ± 555	440 ± 163	1309 ± 73	690 ± 56		5'	30730 ± 501	7780 ± 187	1867 ± 120	726 ± 41
	20	57240 ± 632	850 ± 166	2020 ± 80	743 ± 43		8'	21890 ± 446	6250 ± 180	1427 ± 120	735 ± 52
	21	46880 ± 585	500 ± 165	1530 ± 76	697 ± 50	M19	28	27710 ± 483	3620 ± 172	1287 ± 120	715 ± 56
	22	40870 ± 556	490 ± 163	1330 ± 74	692 ± 55	M21	25	47160 ± 587	3550 ± 172	1976 ± 122	739 ± 42
	23	40050 ± 553	580 ± 164	1349 ± 74	710 ± 56	M22	26	70340 ± 688	5890 ± 183	2976 ± 124	730 ± 30
						M23	27	76760 ± 716	3450 ± 174	3076 ± 125	769 ± 32
						M24	23	41490 ± 558	3550 ± 172	1766 ± 122	731 ± 45
							24	50320 ± 600	3260 ± 171	2036 ± 122	735 ± 40
						M29	24'	44180 ± 572	8010 ± 189	2446 ± 123	760 ± 36
						M34	26'	26970 ± 480	8070 ± 188	1617 ± 121	664 ± 42
							29'	30970 ± 502	8110 ± 189	1837 ± 120	699 ± 40
						M35	34'	38410 ± 547	8300 ± 190	1977 ± 121	662 ± 36

monazites have the lowest ThO<sub>2</sub> content (<3.7 wt %) and the highest UO<sub>2</sub> content (up to 0.35 wt %) (Fig. 14b). This monazite population is mainly distinguished from the other population by its enrichment in Gd and Y (Fig. 14b) and also by the large variation of Y content (Fig. 14c).

Twenty-four analyses have been carried out on 13 monazites belonging to the three distinct textural populations. Calculated individual ages range from 688 ± 53 Ma to 2414 ± 114 Ma with a main population at 765 ± 18 Ma ( $n = 16$ , MSWD = 2.12) (Fig. 15a). The oldest ages (from 815 ± 62 to 2414 ± 114 Ma) are



**Fig. 13.** Backscattered electron images of textural relationships of monazite. (a) Sample A4-5, monazite M7 and M8 included in a UHT garnet (grt<sub>1</sub>). (b) Sample A4-5, monazite M2 and M3 located in the secondary assemblage (spr<sub>2</sub>-crd<sub>2</sub>-opx<sub>2</sub>) produced by the breakdown of UHT garnet (grt<sub>1</sub>). (c) Sample A4-5, monazite M10 and M11 located in the late aggregates of opx<sub>3</sub>-sil<sub>3</sub> formed at the expense of crd<sub>2</sub>. (d) Sample A4-5, close-up view of monazite M11. Needles of sil<sub>3</sub> are partly enclosed in the monazite, suggesting that monazite growth is sub-contemporaneous with the development of opx<sub>3</sub>-sil<sub>3</sub> assemblages. U-Th-Pb dating yields age of  $855 \pm 70$  Ma. (e) Sample An4c, euhedral micro-inclusions of monazites (M18 to M23) included in a UHT garnet (grt<sub>1</sub>). U-Th-Pb ages are reported for each grain. (f) Sample An4c, euhedral monazite M31 included in UHT garnet (grt<sub>1</sub>). U-Th-Pb dating yield ages of  $2499 \pm 85$  Ma and  $2272 \pm 74$  Ma. The Proterozoic age, which is interpreted as a partially reset late Archaean age, is located close to a garnet crack.

systematically preserved in monazites included in UHT porphyroblasts such as garnet (M7-8-4) or orthopyroxene (M1) (Table 11). In contrast, the major middle Neoproterozoic population ( $765 \pm 18$  Ma) is recorded in matrix monazites located in the spr<sub>2</sub>-crd<sub>2</sub>-opx<sub>2</sub> assemblages (M2-3-6-9) and in monazites associated with the opx<sub>3</sub>-sil<sub>3</sub> symplectites (M10-11-12-14) (Table 11).

Monazites included in UHT garnet and orthopyroxene display the same chemical and geochronological characteristics, suggesting that they belong to the same generation, which probably crystallized near or before 2420 Ma (the oldest age preserved in included monazite). Despite the well-known shielding effect of garnet on monazite in the U-Th-Pb system (DeWolf *et al.*, 1993; Montel *et al.*,

1996, 2000; Zhu *et al.*, 1997), the occurrence of numerous cracks in garnet may favour fluid-rock interactions and consequently partial resetting. We suggest that all the intermediate calculated individual ages between about 2.4 Ga and 770 Ma have no geological meaning. Monazites located in the matrix composed of spr<sub>2</sub>-crd<sub>2</sub>-opx<sub>2</sub> do not record Mesoproterozoic to late Archaean ages, and have significantly different chemical compositions. We suggest that these monazites grew during the middle Neoproterozoic event. Textural relationships are not totally conclusive, but we suggest that the crystallization of these monazites is coeval with the development of the matrix assemblage spr<sub>2</sub>-crd<sub>2</sub>-opx<sub>2</sub> in which the monazites are located. Finally, critical microtextural and chemical features suggest that a new monazite generation

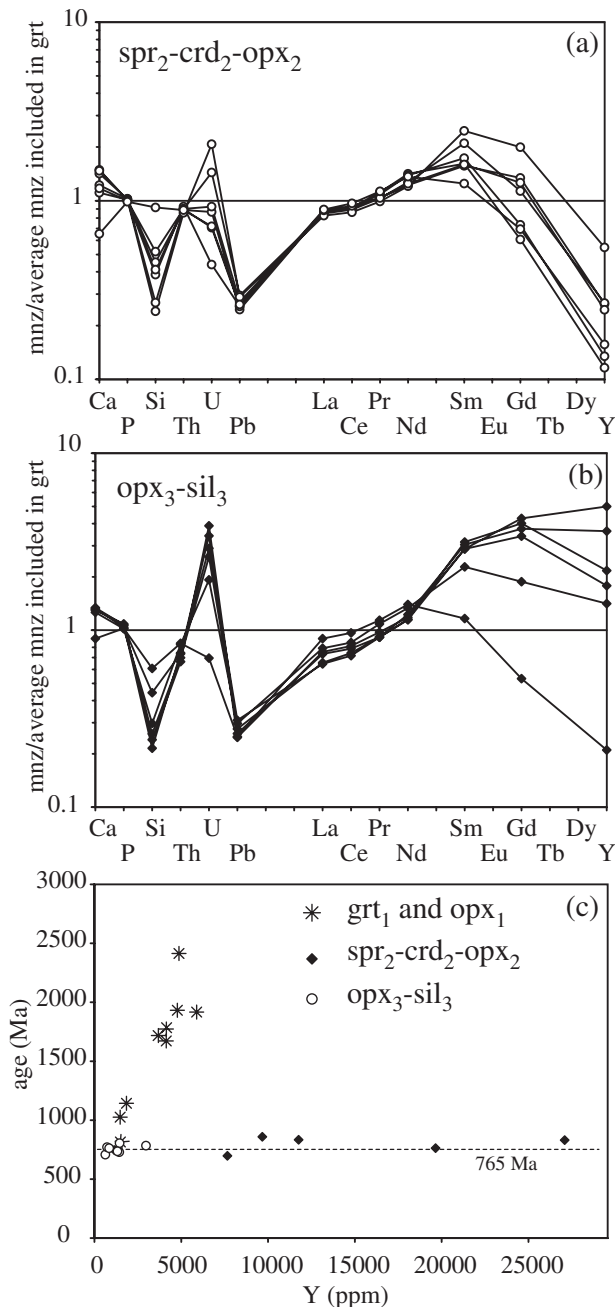


**Fig. 14.** Sample A4-5. (a) Monazite-normalized composition patterns of monazites located in assemblages  $\text{spr}_2\text{-crd}_2\text{-opx}_2$  (the monazite used for the normalization is an average of monazite included in UHT  $\text{grt}_1$ ). (b) Monazite-normalized composition patterns of monazites located in symplectites  $\text{opx}_3\text{-sil}_3$ . (c) Y vs age plot showing the three distinct chemical populations observed in sample A4-5.

crystallized at 770 Ma, at the same time as the  $\text{opx}_3\text{-sil}_3$  symplectites. If this is true it establishes rigorously the absolute timing of the reactions  $\text{crd}_2 = \text{opx}_3 + \text{sil}_3 + \text{qtz}$  and  $\text{crd}_2 + \text{spr}_2 = \text{opx}_3 + \text{sil}_3$  and therefore the

physical conditions under which monazite grew at this time ( $\sim 7$  kbar,  $850^\circ\text{C}$ ).

*Mg-granulite An4c: a well-preserved  $\text{grt-opx-sil-qtz}$  assemblage (stage 1)*

Monazites in this sample are very abundant and occur as perfectly euhedral micro-inclusions ( $< 20 \mu\text{m}$ ) in garnet porphyroblasts ( $\text{grt}_1$ ) (Fig. 13e and f) and as very large and irregular-shaped grains (up to  $400 \mu\text{m}$ ) located in the matrix. In this section, only data obtained on monazite inclusions will be discussed.

Monazite grains included in individual garnets are homogeneous in composition but may differ significantly from garnet to garnet. The  $\text{ThO}_2$ , CaO and  $\text{SiO}_2$  concentrations of the whole monazite population vary in the range 3.1–8.4 wt %, 0.2–1.6 wt % and 0.3–1.8 wt %, respectively. These variations illustrate various degrees of the brabantite ( $2 \text{REE}^{3+} \leftrightarrow \text{Th}^{4+} + \text{Ca}^{2+}$ ) and huttonite ( $\text{REE}^{3+} + \text{P}^{5+} \leftrightarrow \text{Th}^{4+} + \text{Si}^{4+}$ ) substitutions.  $\text{UO}_2$  content is low and homogeneous (0.1–0.3 wt %). REE concentration displays the same large variations from garnet to garnet as the non-REE components. In contrast, monazite micro-inclusions from the same garnet have very homogeneous concentrations of REE and Y and are characterized by very high contents of middle REE (MREE;  $\text{Sm}_2\text{O}_3$  up to 3.7 wt %) and heavy REE (HREE;  $\text{Gd}_2\text{O}_3$  up to 1.9 wt %).

Eighteen analyses were carried out on 12 monazites (Table 11). Individual measurements range from  $1715 \pm 95$  Ma to  $2562 \pm 98$  Ma with a main population at  $2499 \pm 40$  Ma ( $n = 9$ ,  $\text{MSWD} = 0.41$ ) (Fig. 15b). The seven fully armoured micro-inclusions of the same garnet yield late Archaean ages ranging from  $2459 \pm 98$  Ma to  $2562 \pm 99$  Ma, except for one grain (M18), which yields an age of  $1841 \pm 79$  Ma (Fig. 13e). Likewise, the euhedral monazite M31 (Fig. 13f) yields a late Archaean age of  $2499 \pm 85$  Ma and a younger one at  $2272 \pm 82$  Ma, obtained close to a crack affecting the garnet and monazite. It appears clear that monazites that are fully armoured systematically yield maximum ages of about 2.5 Ga, which is in agreement with the maximum age obtained from a monazite included in garnet from sample A4-5.

The perfectly euhedral shape of the monazite included in garnet and the remarkable compositional uniformity of the monazite micro-inclusions in the same garnet porphyroblast exclude the possibility of an inherited origin; rather these features suggest that the monazite is of metamorphic origin. Thus, its crystallization is contemporaneous with garnet ( $\text{grt}_1$ ) growth at 2.5 Ga. We suggest that the younger Palaeoproterozoic ages, as in sample A4-5, have no geological meaning and are a result of a partial resetting.

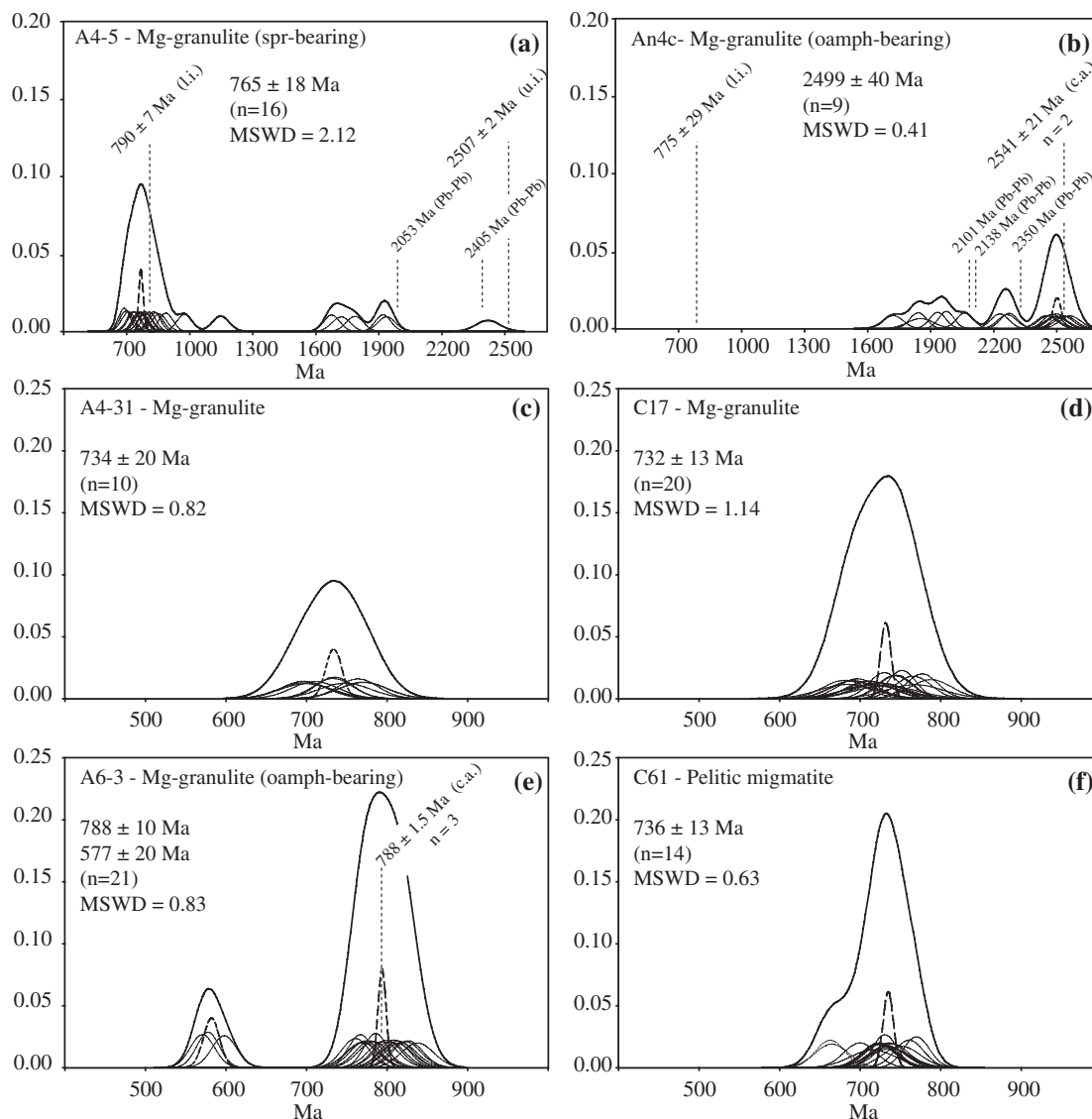


**Fig. 15.** Weighted-histogram representation of the age data from sample (a) A4-5, (b) An4c, (c) A4-31, (d) C17, (e) A6-3 and (f) C61. Each small bell-shaped curve corresponds to Gaussian representation of individual measurement and its  $2\sigma$  error calculated from U, Th, Pb analysis. The bold curve corresponds to the sum of all small bell-shaped curves. The dashed curve is the statistically calculated mean age. There is no unit for vertical axes. In (a), (b) and (e) ID-TIMS ages are represented (intercept ages and  $^{207}\text{Pb}/^{206}\text{Pb}$  for discordant ages) for samples C43, C1 and C6, respectively (Paquette *et al.*, 2004). c.a., concordant ages; u.i., upper intercept age; l.i., lower intercept age; Pb–Pb,  $^{207}\text{Pb}/^{206}\text{Pb}$  apparent age.

*Mg-granulites A4-31 and C17:  $\text{opx}_1\text{-sil}_1\text{-qtz}$  assemblage and well-developed late  $\text{crd}_2$  breakdown reaction*

Monazites in both samples display the same textural and chemical features. They are rare and usually less than  $50\ \mu\text{m}$  in size. They occur exclusively in the matrix associated with  $\text{opx}_3\text{-sil}_3$  assemblages or as inclusion in quartz.

Representative compositions of monazites are presented in Table 10.  $\text{ThO}_2$  abundance varies from 3.2 to 8.6 wt % and  $\text{UO}_2$  from 0.03 to 0.13 wt %. Incorporation of Th in the monazite is largely achieved by the huttonite

substitution. Consequently, these monazites have relatively high  $\text{SiO}_2$  contents, which reach 2 wt %, and low amounts of CaO (<0.8 wt %). In terms of REE concentrations these monazites are characterized by their high contents of  $\text{Sm}_2\text{O}_3$  (0.8–6.5 wt % and 0.9–4.9 wt % for A4-31 and C17, respectively). In most of the monazites of both samples,  $\text{Y}_2\text{O}_3$  contents are negligible.

In sample A4-31, 10 age determinations were obtained on eight monazite crystals (Table 12). Individual ages range between  $697 \pm 62$  Ma and  $771 \pm 60$  Ma and define a unimodal population at  $734 \pm 20$  Ma (MSWD = 0.82)

(Fig. 15c). In sample C17, three monazites were analysed, yielding a total of 20 measurements, which range in age from  $681 \pm 54$  to  $788 \pm 52$  Ma (Table 12). The distribution of the ages defines a unimodal population at  $732 \pm 13$  Ma (MSWD = 1.14), which is in very good agreement with the age obtained for sample A4-31 (Fig. 15d). Because of the extensive development of late assemblages such as cordierite (crd<sub>2</sub>) and orthopyroxene–sillimanite (opx<sub>3</sub>–sil<sub>3</sub>), these ages are interpreted as the age of retrogression.

*Mg-granulite A6-3: grt–opx–sil–qtz peak metamorphic assemblage strongly retrogressed into oamph–crd assemblage*

Monazites from this sample are scarce and occur as sub-hedral grains ( $\sim 50 \mu\text{m}$ ) in the matrix, aligned with the foliation that consists of elongated mono-crystalline quartz, cordierite and orthoamphibole.

ThO<sub>2</sub> and UO<sub>2</sub> contents are homogeneous from 5 to 9.2 wt % and  $<0.6$  wt %, respectively (Table 10). These monazites are characterized by relatively high contents of CaO (0.5–1.6 wt %), SiO<sub>2</sub> (0.1–1.9 wt %) and Y<sub>2</sub>O<sub>3</sub> (0.1–2.6 wt %), implying a significant contribution of the brabantite, huttonite and xenotime cationic exchanges. These monazites are characterized by high concentrations of Gd<sub>2</sub>O<sub>3</sub> and Y<sub>2</sub>O<sub>3</sub> (up to 3.6 and 2.6 wt %, respectively).

Twenty-one measurements were made on five grains (Table 12). The distribution of these ages defines a bimodal population (Fig. 15e). The first population consists of 18 measurements, which range from  $761 \pm 34$  to  $827 \pm 40$  Ma, and the second is defined by only three measurements ranging from  $568 \pm 30$  to  $593 \pm 28$  Ma. The deconvolution of the whole population yields two ages at  $788 \pm 10$  Ma and  $577 \pm 20$  Ma (MSWD = 0.83). The age of 788 Ma is interpreted as the age of initial growth or total resetting during development of the qtz–crd–oamph foliation. The late Neoproterozoic ages were obtained from rims or annealed fractures within the monazite, suggesting a fluid-assisted resetting event at about 580 Ma.

*Pelitic migmatite C61: 'low pressure' partial melting*

Monazites are abundant and occur in both the silica-saturated and -undersaturated layers, usually in the matrix, associated with quartz and plagioclase, and more rarely included in garnet. Their grains vary from 10 to  $150 \mu\text{m}$  in size and have an oval shape, except for the larger monazites, which are characterized by a very irregular shape.

They have a very low ThO<sub>2</sub> content from 0.5 to about 2.0 wt %. To validate the microprobe dating, which is more efficient for highly radioactive crystals, only data obtained on monazites with thorium contents above 20 000 ppm are discussed in this section. The ThO<sub>2</sub> and UO<sub>2</sub> concentrations of these monazites vary, respectively, from 2.5 to 8.7 wt % and 0.4 to 1.0 wt % (Table 10). CaO and SiO<sub>2</sub> contents range from 0.5 to

1.2 wt % and 0.3 to 2.4 wt %, respectively. REE concentrations do not show significant variations within grains and are homogeneous between grains.

Sixteen measurements obtained on 12 grains range from  $662 \pm 36$  to  $769 \pm 32$  Ma (Table 12). Figure 15f shows that calculated ages belong to the same unimodal population, except for two data points at about 660 Ma. Excluding these two youngest ages, a best mean age of  $736 \pm 13$  Ma is obtained with an MSWD of 0.63. This middle Neoproterozoic age is similar to those obtained on the Mg-granulites C17 and A4-31 and is interpreted to reflect the timing of partial melting.

## INTERPRETATION OF THE GEOCHRONOLOGICAL DATA

Integrating *in situ* ages of the monazites, the textural and petrographical observations and the chemical composition reveals that at least two distinct episodes of metamorphic crystallization occurred in the Andriamena unit at 2.5 Ga and 730–790 Ma.

### Early, late Archaean episode of monazite growth: UHT metamorphic conditions

Monazites included in garnet (samples An4c and A4-5) yield the oldest ages in the range 829–2564 Ma. The main population of  $2502 \pm 40$  Ma is obtained on monazites that are fully armoured by garnet (An4c). The lack of evidence for resorption or overgrowths, the homogeneous composition among monazites included in the same garnet, and the ultrahigh-temperature conditions ( $>1050^\circ\text{C}$ ) exclude the possibility that they could be of detrital origin or that they could pre-date the peak metamorphism. Instead, the euhedral shape of some included grains clearly indicates that these grains are metamorphic and that they grew at the same time as garnet. Because garnet forms part of the primary high-grade assemblages in both samples An4c and A4-5 (grt–opx–sil–qtz and spr–grt–qtz, respectively), the 2.5 Ga age is interpreted as the age of the ultrahigh-temperature metamorphism. These data also suggest that the near-isobaric cooling at UHT conditions and a pressure above 10 kbar (stage 1 in Fig. 12) occurred at about 2.5 Ga.

### Second, middle Neoproterozoic episode of monazite growth or resetting: ITD and late IBC

The middle Neoproterozoic event is well recorded in all samples, both the Mg-granulites and the migmatite, except for sample An4c where only data from monazites included in garnet have been discussed. Ages range from  $732 \pm 13$  Ma to  $788 \pm 10$  Ma. The age scattering is significant ( $\sim 50$  Myr), but given the rather poor age precision it is best to consider that these ages belong to

a single middle Neoproterozoic thermal event. However, it is also possible that this time interval embodies distinct thermal pulses at 790 Ma (coeval with a mafic–ultramafic magmatism; Guérot *et al.*, 1993) and at 730 Ma.

The timing of the crystallization of  $\text{spr}_2\text{-crd}_2\text{-opx}_2$  at the expense of the late Archaean UHT assemblages (Fig. 12) is constrained mainly by sample A4-5. According to the age and chemical characteristics of the monazite located in the  $\text{spr}_2\text{-crd}_2\text{-opx}_2$  assemblage, we conclude that a new episode of monazite growth occurred at about 770 Ma.

Monazites from samples A4-31 and C17 yield middle Neoproterozoic ages ( $734 \pm 20$  Ma and  $732 \pm 13$  Ma, respectively), but the conditions in which monazite grew at this time are more uncertain. However, the widespread development of the late  $\text{opx}_3\text{-sil}_3$  assemblage suggests that the growth or resetting of monazite may have occurred at lower-than-peak conditions of metamorphism. This possibility is confirmed by sample A4-5, in which critical textural relationships, chemical composition and dating clearly indicate that a new episode of monazite crystallization occurred after the late Archaean peak metamorphism. Indeed, monazite grew at the same time as the late development of  $\text{opx}_3\text{-sil}_3 \pm \text{qtz}$  assemblage, which constrains the late  $\text{crd}_2$  breakdown ( $\sim 6$  kbar,  $850^\circ\text{C}$ ) and the IBC (Fig. 12) at about 770 Ma. Mg-granulite C6 displays an intense deformation associated with a hydrated retrogression responsible for the breakdown of initial UHT garnet into orthoamphibole and cordierite. We suggest that the age of  $788 \pm 10$  Ma reflects the timing of this hydrated deformation, which is coeval with the near-isobaric cooling from  $\sim 7\text{--}8$  kbar and  $900^\circ\text{C}$  to  $\sim 5$  kbar and  $650^\circ\text{C}$ . Monazite from the pelitic migmatite also yields a middle Neoproterozoic age ( $736 \pm 13$  Ma), which is interpreted as the timing of partial melting at peak metamorphic conditions of  $850^\circ\text{C}$  and 7 kbar or of late back melting reactions at  $700 \pm 50^\circ\text{C}$  and  $6 \pm 1$  kbar.

In conclusion, the secondary assemblage, interpreted as the result of an ITD from about 10 to 7 kbar at  $T > 900^\circ\text{C}$ , and a low-pressure isobaric cooling  $P\text{--}T$  path at about 6–7 kbar (Fig. 12), inferred from three distinct rock types, is ascribed to the same middle Neoproterozoic event (730–790 Ma).

### Comparison with ID-TIMS data

Three Mg-granulites from the same localities as the studied samples have been dated by conventional isotopic dilution–thermal ionization mass spectrometry (ID-TIMS) (Paquette *et al.*, 2004). Sample C43, the petrology of which is described in this study, is a sapphirine-bearing rock comparable with sample A4-5 in terms of mineralogy and metamorphic evolution. The analysed monazites are strongly discordant and define a discordia with an upper intercept at  $2507 \pm 2$  Ma and a lower intercept

at  $790 \pm 7$  Ma. Sample C1 preserves relics of UHT assemblages (grt, opx, sil), which are retrogressed into orthoamphibole–cordierite. This sample is equivalent to the studied sample An4c. A fraction of analysed monazite is concordant at  $2541 \pm 1$  Ma. Strongly discordant monazites define a poor alignment with a lower intercept at  $775 \pm 29$  Ma. Sample C6 is similar to A6-3. It is a highly deformed garnet–cordierite–orthoamphibole-bearing rock, in which the analysed monazites give a concordant age of  $788 \pm 2$  Ma.

ID-TIMS ages, including intercepts and apparent  $^{207}\text{Pb}/^{206}\text{Pb}$  ages for discordant monazites, are reported in the EMP age histograms (Fig. 15a for sample C43, Fig. 15b for sample C1 and Fig. 15e for sample C6). Isotopic U–Pb dating records two main events at 2.51–2.54 Ga and 770–790 Ma, consistent with the EMP ages. However, the 730 Ma event inferred from three samples by EMP dating was not elucidated by ID-TIMS. Even if we are not strictly comparing the same dated monazite grains or rocks, it is noteworthy that meaningless EMP ages and TIMS discordant ages were reported for the same type of rocks (spr-bearing: A4-5 and An4c; grt–opx–sil-bearing: C43 and C6). We suggest that both chemical and isotopic apparent ages result from the mixing of micron- or nanometre-scale domains of 2.5 Ga and 790 Ma age, as suggested by Seydoux-Guillaume *et al.* (2003) and Paquette *et al.* (2004).

### Variations in composition

In addition to textural observations and *in situ* dating, monazite chemical composition may be an excellent indicator of multiphase episodes of monazite crystallization in polymetamorphic context (Foster *et al.*, 2000). Textural relationships from sample A4-5 allow us to distinguish three monazite generations: grains included in garnet (grt<sub>1</sub>), matrix grains coexisting with  $\text{spr}_2\text{-crd}_2\text{-opx}_2$  assemblages and late  $\text{opx}_3\text{-sil}_3$  symplectites. Each of these textural types has a distinct chemical composition. Monazites located in the  $\text{spr}_2\text{-crd}_2\text{-opx}_2$  assemblage are the most depleted in Sm, Gd and Y (Fig. 14a). In contrast, monazites associated with  $\text{opx}_3\text{-sil}_3$  assemblage are the most enriched in Sm, Gd and Y and display the lowest Th/U ratio (Fig. 14b).

## DISCUSSION

### Regional correlation

U–Th–Pb EMP dating of monazite reveals the occurrence of two major metamorphic events at about 2.5 Ga and 730–790 Ma.

(1) The late Archaean age is interpreted as the age of the UHT metamorphism ( $1000 \pm 50^\circ\text{C}$  and  $10.5 \pm 1.5$  kbar) recorded in lenses of Mg-granulites. Similar

late Archaean U–Pb zircon ages ranging from  $2494 \pm 4$  Ma to  $2518 \pm 5$  Ma have been obtained on granodioritic, tonalitic and gabbroic gneisses from the Maevatanana unit and the Aloatra–Beforona unit (Tucker *et al.*, 1997), which are equivalent to the Andriamena unit (Bésairie, 1963; Collins & Windley, 2002). These ages are interpreted as emplacement ages (Tucker *et al.*, 1999). Granodioritic gneisses from the basement located just south of the Andriamena unit display the same ages, which range from 2510 to 2550 Ma [sensitive high-resolution ion microprobe (SHRIMP) and Pb–Pb evaporation] and are interpreted as emplacement ages (Kröner *et al.*, 2000). According to the isotopic signature, Tucker *et al.* (1999) suggested that the gneisses are mantle-derived magmas mixed with middle Archaean crust. The extreme thermal perturbation responsible for UHT metamorphism is probably due to crystallization of the gneisses at lower-crustal levels during the emplacement in pre-existing continental crust of mantle-derived magma. The tectonic setting, however, wherein such high thermal perturbation occurred remains unknown.

(2) The second thermal event (730–790 Ma) corresponds to a phase of partial melting associated with granulite-facies metamorphism at 7 kbar and 850–900°C. This second phase is coeval with the emplacement of a huge volume of mafic to ultramafic rocks in the Andriamena and Maevatanana unit at 780–790 Ma (Guérrot *et al.*, 1993; Tucker *et al.*, 1999) and granitoids in the late Archaean basement at 720–820 Ma (Kröner *et al.*, 2000). The geochemical signature of these middle Neoproterozoic rocks is interpreted as the result of contamination of mantle-derived magmas with the late Archaean continental crust in an Andean-type continental magmatic arc setting (Handke *et al.*, 1999; Tucker *et al.*, 1999; Kröner *et al.*, 2000). Metamorphic conditions of ~7 kbar and 850–900°C are in good agreement with a high-grade metamorphism produced by magmatic underplating at the base of a magmatic arc (Bohlen, 1991), as described in well-recognized arc settings such as the Kohistan island arc (Bard, 1983), the Chile Coastal Cordillera (Lucassen & Franz, 1996) or the French Massif Central (Lardeaux *et al.*, 2001). Furthermore, the middle Neoproterozoic near-IBC cooling is also consistent with a model of magmatic accretion at the base of a crust of normal thickness, followed by a thermal relaxation to a normal crustal geotherm (Ellis, 1987).

Exposure at the surface of such high-grade metamorphic and magmatic rocks requires a subsequent tectonic event (Ellis, 1987), which may correspond to late Neoproterozoic–Cambrian (530–500 Ma) continental convergence during the final amalgamation of Gondwana. Thrusting and upright folding during crustal shortening achieved exhumation of the root of the magmatic arc (Goncalves *et al.*, 2003).

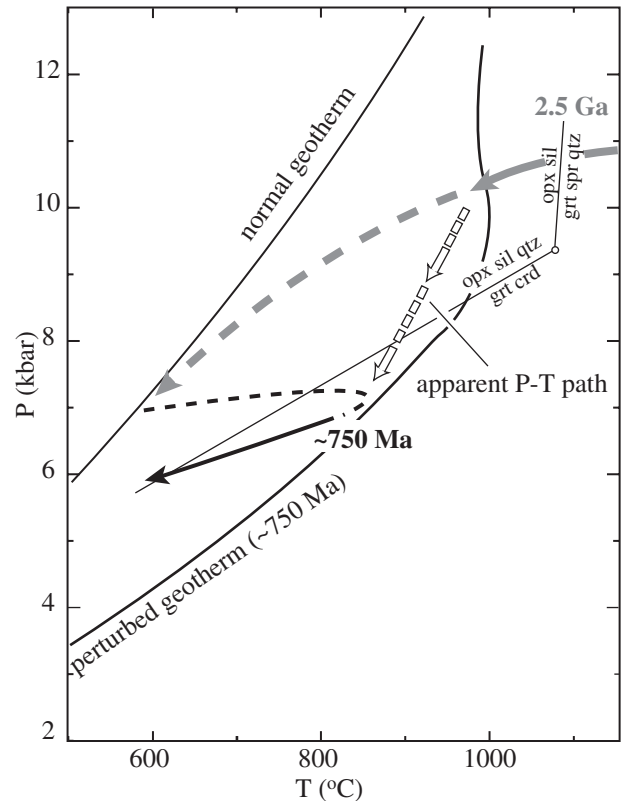


**Fig. 16.** Interpretative  $P$ – $T$  path constructed in view of petrological, geochronological and geodynamic constraints. In this model, the petrographical ITD is interpreted as an apparent  $P$ – $T$  path with no geological meaning. It results from the partial equilibration of the persistent 2.5 Ga UHT assemblages at lower pressure during the middle Neoproterozoic event. The metamorphic reactions (white arrows) occurred without the sample having been subjected to the equilibrium  $P$ – $T$  conditions of the observed reactions. Continuous bold grey arrow indicates 2.5 Ga  $P$ – $T$  evolution inferred from petrographical observations. Dashed bold grey line indicates hypothetical 2.5 Ga  $P$ – $T$  evolution not recorded by mineral changes. Continuous black arrow indicates ~750 Ma  $P$ – $T$  evolution inferred from petrographical observations. Dashed black line indicates hypothetical ~750 Ma  $P$ – $T$  evolution not recorded by mineral changes.

### Significance of a petrographical $P$ – $T$ path in a polymetamorphic context

Detailed monazite dating indicates that the continuous retrograde  $P$ – $T$  path inferred from a suite of mineral reactions within Mg-granulites from Andriamena does not represent a single cooling event. Rather it formed as the result of superposition of two high-grade events well separated in time, at 2.5 Ga and 730–790 Ma, corresponding to the ages of the UHT metamorphism (stage 1) and the UHT–ITD path (stage 2) followed by the near-IBC path at lower pressure (stage 3), respectively (Fig. 16). It is obvious that high-grade conditions, i.e.  $>850^{\circ}\text{C}$ , at lower-crustal levels cannot persist for 1–7 Gyr. Therefore, we suggest that the Mg-granulites underwent cooling to the stable geotherm following the

late Archaean UHT metamorphism (Fig. 16). There is no petrological evidence for this late Archaean cooling event probably because the cooling was relatively rapid compared with the rate of mass transfer reactions under anhydrous conditions.

After a long period of residence ( $\sim 1.7$  Gyr) under normal geothermal conditions at mid- to lower-crustal levels, a second high-grade event occurred around 750 Ma, which led to the near-isobaric heating and cooling  $P$ - $T$  path inferred from the pelitic migmatites and Mg-granulites (Fig. 16). This event is also responsible for the re-equilibration of the refractory persistent late Archaean 'high-pressure' assemblages at lower pressure, producing an apparent ITD path with no tectonic significance. Although the decompression is well recorded by a continuous sequence of reactions, we suggest that these reactions were produced outside their stability field without the sample having been subjected to the equilibrium  $P$ - $T$  conditions of the observed reactions. The recognition of a discontinuous and apparent  $P$ - $T$  path in the polyphase UHT granulites from Madagascar means that caution must be used in tectonic interpretations inferred from  $P$ - $T$  paths without any suitable dating, as emphasized by Hand *et al.* (1992), Vernon (1996) and Raith & Harley (1998).

## ACKNOWLEDGEMENTS

The fieldwork of C.N. and P.G. was financially supported by the 'Service des Relations Internationales' from the Université Blaise Pascal, Clermont-Ferrand. Many thanks are also due to the geology laboratory of the University of Antananarivo (Madagascar) for their logistic support. Michel Veschambre is thanked for her assistance with the electron microprobe. The authors are grateful to Aphrodite Indares, Peter S. Dahl, David Pattison, Patrick O'Brien, Andreas Möller and Thomas Zack for their helpful reviews on an initial version of the manuscript consisting of two parts. Ron Frost is also thanked for his careful reviews and editorial handling of the manuscripts.

## REFERENCES

- Ancey, M., Bastenaire, F. & Tixier, R. (1978). Application des méthodes statistiques en microanalyse. In: Maurice, F., Menyand, L. & Tixier, R. (eds) *Microanalyse, Microscopie Électronique à Balayage*. Orsay: Les éditions du physicien, pp. 323–347.
- Aranovich, L. Y. & Berman, R. G. (1996). Optimized standard state and solution properties of minerals. part II. Comparisons, predictions, and applications. *Contributions to Mineralogy and Petrology* **126**, 25–37.
- Audibert, N., Hensen, B. J. & Bertrand, P. (1995). Experimental study of phase relations involving osumilite in the system  $K_2O$ - $FeO$ - $MgO$ - $Al_2O_3$ - $SiO_2$ - $H_2O$  at high pressure and temperature. *Journal of Metamorphic Geology* **13**, 331–344.
- Bard, J. P. (1983). Metamorphism of an obducted island arc: example of the Kohistan sequence (Pakistan) in the Himalayan Collided range. *Earth and Planetary Science Letters* **65**, 133–144.
- Bertrand, P., Ellis, D. J. & Green, H. (1991). The stability of sapphirine-quartz and hypersthene-sillimanite-quartz assemblages: an experimental investigation in the system  $FeO$ - $MgO$ - $Al_2O_3$ - $SiO_2$  under  $H_2O$  and  $CO_2$  conditions. *Contributions to Mineralogy and Petrology* **108**, 55–71.
- Bertrand, P., Ouzegane, K. H. & Kienast, J. R. (1992).  $P$ - $T$ - $X$  relationships in the Precambrian Al-Mg-rich granulites from In Ouzzal, Algeria. *Journal of Metamorphic Geology* **10**, 17–31.
- Bésairie, H. (1963). *Description géologique du massif ancien de Madagascar. Premier volume, Centre Nord et Centre Nord-Est*. Tananarive: Service Géologique.
- Bohlen, S. R. (1991). On the formation of granulites. *Journal of Metamorphic Geology* **9**, 223–229.
- Bose, S., Fukuoka, M., Sengupta, P. & Dasgupta, S. (2000). Evolution of high-Mg-Al granulites from Sunkarametta, Eastern Ghats, India: evidence for a lower crustal heating-cooling trajectory. *Journal of Metamorphic Geology* **18**, 223–240.
- Caen-Vachette, M. (1979). Le Précambrien de Madagascar. Radiochronométrie par isochrones Rb-Sr sur roches totales. *Revue de Géologie Dynamique et de Géographie Physique* **21**, 331–338.
- Carrington, D. P. & Harley, S. L. (1995). Partial melting and phase relations in high-grade metapelites: an experimental petrogenetic grid in the KFMASH system. *Contributions to Mineralogy and Petrology* **120**, 270–291.
- Chatterjee, N. D. & Schreyer, W. (1972). The reaction enstatite + sillimanite = sapphirine + quartz in the system  $MgO$ - $Al_2O_3$ - $SiO_2$ . *Contributions to Mineralogy and Petrology* **36**, 49–62.
- Collins, A. S. & Windley, B. F. (2002). The tectonic evolution of central and northern Madagascar and its place in the final assembly of Gondwana. *Journal of Geology* **110**, 325–340.
- Collins, A. S., Razakamanana, T. & Windley, B. F. (2000). Neoproterozoic extensional detachment in central Madagascar: implications for the collapse of the East African Orogen. *Geological Magazine* **137**, 39–51.
- Connolly, J. A. D. (1990). Multivariable phase diagrams: an algorithm based on generalized thermodynamics. *American Journal of Science* **290**, 666–718.
- DeWolf, C. P., Belshaw, N. & O'Nions, R. K. (1993). A metamorphic history from micron-scale  $^{207}Pb/^{206}Pb$  chronometry of Archean monazite. *Earth and Planetary Science Letters* **120**, 207–220.
- Droop, G. T. R. (1989). Reaction history of garnet-sapphirine granulites and conditions of Archaean high-pressure granulite-facies metamorphism in the Central Limpopo Mobile Belt, Zimbabwe. *Journal of Metamorphic Geology* **7**, 383–403.
- Ellis, D. J. (1987). Origin and evolution of granulites in normal and thickened crusts. *Geology* **15**, 167–170.
- Fitzsimons, I. C. W. & Harley, S. L. (1994). Disequilibrium during retrograde cation exchange and recovery of peak metamorphic temperatures: a study of granulites from Antarctica. *Journal of Petrology* **35**, 543–576.
- Foster, G., Kinny, P., Vance, D., Prince, C. & Harris, N. (2000). The significance of monazite U-Th-Pb age data in metamorphic assemblages; a combined study of monazite and garnet chronometry. *Earth and Planetary Science Letters* **181**, 237–340.
- Gardien, V., Thompson, A. B., Grujic, D. & Ulmer, P. (1995). Experimental melting of biotite + plagioclase + quartz  $\pm$  muscovite assemblages and implications for crustal melting. *Journal of Geophysical Research* **100**, 15581–15591.
- Goncalves, P., Nicollet, C. & Lardeaux, J. M. (2003). Finite strain pattern in Andriamena unit (north-central Madagascar): evidence

- for late Neoproterozoic–Cambrian thrusting during continental convergence. *Precambrian Research* **123**, 135–157.
- Goscombe, B. (1992). High-grade reworking of Central Australian granulites: metamorphic evolution of the Arunta complex. *Journal of Petrology* **33**, 917–962.
- Gu errot, C., Cocherie, A. & Ohnenstetter, M. (1993). Origin and evolution of the West Andriamena Pan-African mafic–ultramafic complex in Madagascar as shown by U–Pb, Nd isotopes and trace element constraints. EUG VIII, Strasbourg, France. *Terra Abstracts* **5**, 387.
- Hand, M., Dirks, P. H. G. M., Powell, R. & Buick, I. S. (1992). How well established is isobaric cooling in Proterozoic orogenic belts? An example from the Arunta inlier, central Australia. *Geology* **20**, 649–652.
- Handke, M. J., Tucker, R. D. & Ashwal, L. D. (1999). Neoproterozoic continental arc magmatism in west–central Madagascar. *Geology* **27**, 351–354.
- Harley, S. L. (1985). Paragenetic and mineral–chemical relationships in orthoamphibole-bearing gneisses from Enderby Land, east Antarctica: a record of Proterozoic uplift. *Journal of Metamorphic Geology* **3**, 179–200.
- Harley, S. L. (1998a). On the occurrence and characterization of ultrahigh-temperature crustal metamorphism. In: Treolar, P. J. & O’Brien, P. J. (eds) *What Drives Metamorphism and Metamorphic Reactions?* Geological Society, London, *Special Publications* **138**, 81–107.
- Harley, S. L. (1998b). Ultrahigh temperature granulite metamorphism (1050°C, 12 kbar) and decompression in garnet (Mg70)–orthopyroxene–sillimanite gneisses from the Rauer Group, East Antarctica. *Journal of Metamorphic Geology* **16**, 541–562.
- Harley, S. L. & Green, D. H. (1982). Garnet–orthopyroxene barometry for granulites and peridotites. *Nature* **300**, 697–701.
- Harley, S. L., Hensen, B. J. & Sheraton, J. W. (1990). Two-stage decompression in orthopyroxene–sillimanite granulites from Forefinger Point, Enderby Land, Antarctica: implication for the evolution of the Archaean Napier Complex. *Journal of Metamorphic Geology* **8**, 591–613.
- Hensen, B. J. (1986). Theoretical phase relations involving cordierite and garnet revisited: the influence of oxygen fugacity on the stability of sapphirine and spinel in the system Mg–Fe–Al–Si–O. *Contributions to Mineralogy and Petrology* **92**, 362–367.
- Hensen, B. J. & Harley, S. L. (1990). Graphical analysis of *P–T–X* relations in granulite facies metapelites. In: Ashworth, J. R. & Brown, M. (eds) *High-temperature Metamorphism and Crustal Anatexis*. Mineralogical Society Series **2**, 19–56.
- Hisada, K. & Miyano, T. (1996). Petrology and microthermometry of aluminous rocks in the Botswana Limpopo Central Zone: evidence for isothermal decompression and isobaric cooling. *Journal of Metamorphic Geology* **14**, 183–197.
- Hodges, K. V. & Crowley, P. D. (1985). Error estimation and empirical geothermobarometry for pelitic systems. *American Mineralogist* **70**, 702–709.
- Holland, T. J. B. & Powell, R. (1998). An internally-consistent thermodynamic dataset for phases of petrological interest. *Journal of Metamorphic Geology* **16**, 309–343.
- Jercinovic & Williams (2004). Analytical perils (and progress) in electron microprobe trace element analysis applied to geochronology: background acquisition, interferences, and beam irradiation effects. *American Mineralogist* (in press).
- Koziol, A. M. & Newton, R. C. (1988). Redetermination of the anorthite breakdown reaction and improvement of the plagioclase–garnet–Al<sub>2</sub>SiO<sub>5</sub>–quartz barometer. *American Mineralogist* **73**, 216–223.
- Kriegsman, L. M. (2001). Partial melting, partial melt extraction and partial back reaction in anatexitic migmatites. *Lithos* **56**, 75–96.
- Kriegsman, L. M. & Hensen, B. J. (1998). Back reaction between restite and melt: implication for geothermobarometry and pressure–temperature paths. *Geology* **26**, 1111–1114.
- Kriegsman, L. M. & Schumacher, J. C. (1999). Petrology of sapphirine-bearing and associated granulites from central Sri Lanka. *Journal of Petrology* **40**, 1211–1239.
- Kr oner, A., Hegner, E., Collins, A. S., Windley, B. F., Brewer, T. S., Razakamanana, T. & Pidgeon, R. T. (2000). Age and magmatic history of the Antananarivo block, Central Madagascar, as derived from zircon geochronology and Nd isotopic systematics. *American Journal of Science* **300**, 251–288.
- Lardeaux, J. M., Ledru, P., Daniel, I. & Duchene, S. (2001). The Variscan French Massif Central—a new addition to the ultra-high pressure metamorphic ‘club’: exhumation processes and geodynamic consequences. *Tectonophysics* **332**, 143–167.
- Lucassen, F. & Franz, G. (1996). Magmatic arc metamorphism: petrology and temperature history of metabasic rocks in the Coastal Cordillera of northern Chile. *Journal of Metamorphic Geology* **14**, 249–265.
- Martelat, J. E. (1998). Evolution thermom ecanique de la cro ute inf erieure du Sud de Madagascar. Ph.D. thesis, Universit e Blaise Pascal, Clermont-Ferrand.
- Martelat, J. E., Lardeaux, J. M., Nicollet, C. & Rakotondrzafy, R. (2000). Strain pattern and late Precambrian deformation history in southern Madagascar. *Precambrian Research* **102**, 1–20.
- McDade, P. & Harley, S. L. (2001). A petrogenetic grid for aluminous granulite facies metapelites in the KFMASH system. *Journal of Metamorphic Geology* **19**, 45–59.
- Montel, J. M., Veschambre, M. & Nicollet, C. (1994). Datation de la monazite   la microsonde  lectronique. (Dating monazite using electron microprobe.) *Comptes Rendus de l’Acad mie des Sciences* **318**, 1489–1495.
- Montel, J. M., Foret, S., Veschambre, M., Nicollet, N. & Provost, A. (1996). Electron microprobe dating of monazite. *Chemical Geology* **131**, 37–53.
- Montel, J. M., Kornprobst, J. & Vielzeuf, D. (2000). Preservation of old U–Th–Pb ages in shielded monazite: example from the Beni Bousera Hercynian kinzigites (Morocco). *Journal of Metamorphic Geology* **18**, 335–342.
- Newton, R. C. (1972). An experimental determination of the high-pressure stability limits of magnesian cordierite under wet and dry conditions. *Journal of Geology* **80**, 398–420.
- Nicollet, C. (1988). M etabasites granulitiques, anorthosites et roches associ ees de la cro ute inf erieure: exemple pris   Madagascar et dans le Massif Central Fran ais. Arguments en faveur d’un m etamorphisme associ    l’extension lithosph erique. Th ese d’ tat, Universit e Blaise-Pascal, Clermont-Ferrand.
- Nicollet, C. (1990). Crustal evolution of the granulites of Madagascar. In: Vielzeuf, D. & Vidal, P. (eds) *Granulites and Crustal Evolution*. Dordrecht: Kluwer Academic, pp. 291–310.
- Nicollet, C., Montel, J. M., Foret, S., Martelat, J. E., Lardeaux, J. M. & Rakotondrzafy, R. (1997). E-probe monazite dating: an excellent tool for dating uplift and polymetamorphic events; examples of the granulites from Madagascar. In: Cox, R. & Ashwal, L. D. (eds) *Proceedings of the UNESCO–IUGS–IGCP 348/368 International Workshop on Proterozoic Geology of Madagascar, Antananarivo, Madagascar*. UNESCO–IUGS–IGCP.
- Ouzegane, K., Guiraud, M. & Kienast, J. R. (2003). Prograde and retrograde evolution in high-temperature corundum granulites (FMAS and KFMASH systems) from In Ouzzal terrane (NW Hoggar, Algeria). *Journal of Petrology* **44**, 517–545.

- Paquette, J. L. & Nédélec, A. (1998). A new insight into Pan-African tectonics in the East–West Gondwana collision zone by U–Pb zircon dating of granites from central Madagascar. *Earth and Planetary Science Letters* **155**, 45–56.
- Paquette, J. L., Goncalves, P., Nicollet, C. & Devouard, B. (2004). Micro-drilling ID-TIMS U–Pb dating of single monazites: a new method to unravel complex poly-metamorphic evolutions. Application to the UHT granulites of Andriamena (north–central Madagascar). *Contributions to Mineralogy and Petrology* **156**, 656–669.
- Pattison, D. R. M. & Bégin, N. J. (1994). Zoning patterns in orthopyroxene and garnet in granulites: implications for geothermobarometry. *Journal of Metamorphic Geology* **12**, 387–410.
- Pattison, D. R. M., Chacko, T., Farquhar, J. & McFarlane, C. R. M. (2003). Temperatures of granulite facies metamorphism: constraints from experimental phase equilibria and thermobarometry corrected for retrograde exchange. *Journal of Petrology* **44**, 867–900.
- Raith, J. G. & Harley, S. L. (1998). Low-*P*/high-*T* metamorphism in the Okiep Copper District, western Namaqualand, South Africa. *Journal of Metamorphic Geology* **16**, 281–305.
- Raith, M., Karmakar, S. & Brown, M. (1997). Ultra-high-temperature metamorphism and multistage decompressional evolution of sapphirine granulites from the Palni Hill Ranges, southern India. *Journal of Metamorphic Geology* **15**, 379–399.
- Rickers, K., Raith, M. & Dasgupta, S. (2001). Multistage reaction textures in xenolithic high-MgAl granulites at Anakapalle, Eastern Ghats Belt, India: examples of contact polymetamorphism and infiltration-driven metasomatism. *Journal of Metamorphic Geology* **19**, 561–580.
- Sandiford, M., Neall, F. B. & Powell, R. (1987). Metamorphic evolution of aluminous granulites from Labwor Hills, Uganda. *Contributions to Mineralogy and Petrology* **95**, 217–225.
- Sengupta, P., Sen, J., Dasgupta, S., Raith, M., Bhui, U. K. & Ehl, J. (1999). Ultra-high temperature metamorphism of metapelitic granulites from Kondapalle, Eastern Ghats Belt: implication for the Indo-Antarctic correlation. *Journal of Petrology* **40**, 1065–1087.
- Seydoux-Guillaume, A.-M., Goncalves, P., Wirth, R. & Deutsch, A. (2003). Transmission electron microscope study of polyphase and discordant monazites: site-specific specimen preparation using the focused ion beam technique. *Geology* **31**, 973–976.
- Tucker, R. D., Ashwal, L. D., Handke, M. J. & Hamilton, M. A. (1997). A geochronologic overview of the Precambrian rocks of Madagascar: a record from the Middle Archaean to the Late Neoproterozoic. In: Cox, R. & Ashwal, L. D. (eds) *Proceedings of the UNESCO-IUGS-IGCP 348/368 International Workshop on Proterozoic Geology of Madagascar, Antananarivo, Madagascar, 5*. UNESCO-IUGS-IGCP, p. 99.
- Tucker, R. D., Ashwal, L. D., Handke, M. J., Hamilton, M. A., Grange, M. L. & Rambeloson, R. A. (1999). U–Pb geochronology and isotope geochemistry of the Archaean and Proterozoic rocks of north–central Madagascar. *Journal of Geology* **107**, 135–153.
- Van Reenen, D. D. (1986). Hydration of cordierite and hypersthene and a description of the retrograde orthoamphibole isograd in the Limpopo belt, South Africa. *American Mineralogist* **71**, 900–915.
- Vernon, R. H. (1972). Reactions involving hydration of cordierite and hypersthene. *Contributions to Mineralogy and Petrology* **35**, 125–137.
- Vernon, R. H. (1996). Problems with inferring *P–T–t* paths in low-*P* granulite facies rocks. *Journal of Metamorphic Geology* **14**, 143–153.
- Vielzeuf, D. & Holloway, J. R. (1988). Experimental determination of the fluid-absent melting relations in the pelitic system. *Contributions to Mineralogy and Petrology* **98**, 257–276.
- Vielzeuf, D. & Schmidt, M. W. (2001). Melting reactions in hydrous systems revisited: application to metapelites, metagreywackes and metabasalts. *Contributions to Mineralogy and Petrology* **141**, 251–267.
- White, R. W., Powell, R. & Holland, T. J. B. (2001). Calculation of partial melting equilibria in the system Na<sub>2</sub>O–CaO–K<sub>2</sub>O–FeO–MgO–Al<sub>2</sub>O<sub>3</sub>–SiO<sub>2</sub>–H<sub>2</sub>O (NCKFMASH). *Journal of Metamorphic Geology* **19**, 139–153.
- Williams, M. L., Jercinovic, M. J. & Terry, M. P. (1999). Age mapping and dating of monazite on the electron microprobe: deconvoluting multistage tectonic histories. *Geology* **27**, 1023–1026.
- Zhu, X. K., O’Nions, R. K., Belshaw, N. S. & Gibb, A. J. (1997). Lewisian crustal history from in situ SIMS mineral chronometry and related metamorphic textures. *Chemical Geology* **136**, 205–218.